

# Defocus based phase imaging for quantifying electromagnetic edge effects in photomasks

*Aamod Shanker  
Laura Waller, Ed.  
Andrew R. Neureuther, Ed.*



Electrical Engineering and Computer Sciences  
University of California at Berkeley

Technical Report No. UCB/EECS-2014-105

<http://www.eecs.berkeley.edu/Pubs/TechRpts/2014/EECS-2014-105.html>

May 16, 2014

Copyright © 2014, by the author(s).  
All rights reserved.

Permission to make digital or hard copies of all or part of this work for personal or classroom use is granted without fee provided that copies are not made or distributed for profit or commercial advantage and that copies bear this notice and the full citation on the first page. To copy otherwise, to republish, to post on servers or to redistribute to lists, requires prior specific permission.

### Acknowledgement

Deeply indebted to Professors Laura Waller and Andy Neureuther for providing the vision leading to the ideas presented in this work. Many thanks also to Martin Sczyrba, Brid Connolly and others at AMTC, Dresden for support and collaboration on the experimental results. Final word of gratitude to the body of thinkers and doers that have kept the wheels of inquiry and invention moving along, for we can see far only because we stand on the shoulders of giants.

---

**Defocus based phase imaging for quantifying electromagnetic edge effects in photomasks**  
by Aamod Shanker

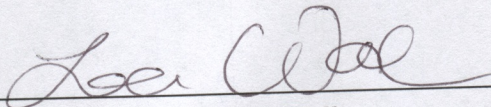
---

**Research Project**

Submitted to the Department of Electrical Engineering and Computer Sciences, University of California at Berkeley, in partial satisfaction of the requirements for the degree of **Master of Science, Plan II.**

Approval for the Report and Comprehensive Examination:

**Committee:**

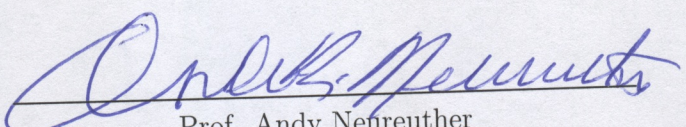
  
\_\_\_\_\_

Prof. Laura Waller  
Research Advisor

          MAY 16, 2014          

Date

\*\*\*\*\*

  
\_\_\_\_\_

Prof. Andy Neureuther  
Second Reader

          May 16, 2014          

Date

---

**Defocus based phase imaging for analyzing edge effects in  
photomasks**

by Aamod Shanker

---

**Research Project**

Submitted to the Department of Electrical Engineering and Computer Sciences, University of California at Berkeley, in partial satisfaction of the requirements for the degree of **Master of Science, Plan II**.

Approval for the Report and Comprehensive Examination:

**Committee:**

---

Prof. Laura Waller  
Research Advisor

---

Date

\* \* \* \* \*

---

Prof. Andy Neureuther  
Second Reader

---

Date

## Abstract

Defocus based phase imaging for quantifying electromagnetic edge effects in photomasks

by

Aamod Shanker

Master of Science in Electrical Engineering

University of California, Berkeley

Professor Laura Waller, Chair

The edges of absorbing regions used to define features on photomasks have inherent electromagnetic diffraction effects that limit the focus tolerance during projection printing. In this work it is shown that the thin mask boundary layers used to characterize these effects can be directly measured by capturing through-focus aerial images, a routine procedure for local quality inspection during mask fabrication. The Transport of Intensity phase imaging method is used to recover quantitative phase from a stack of intensity images, the phase near feature edges directly corresponding to edge effects at the mask. We discover that the Transport of Intensity solver produces errors in the solved phase near sharp corners due to strong curl effects in the power flow, and an iterative solver is developed to remedy the artifacts. Using the improved algorithm, polarization-dependent edge effects are observed experimentally in the quantitative phase images for both OMOG and ATT-PSM masks. The measured edge effects correspond to 20nm wide imaginary valued boundary layers for ATT-PSM, and half that for OMOG masks, values which agree with those predicted by full-wave simulations in literature. Finally, the TIE is extended for the case of general illumination, and it is shown that the phase can be recovered from intensity measurements at a single focal plane by illumination patterning.

# Contents

<b>Contents</b>	<b>i</b>
<b>List of Figures</b>	<b>iii</b>
<b>1 Introduction</b>	<b>1</b>
1.1 Electromagnetic edge effects in photomasks . . . . .	1
1.2 Characterizing edge effects . . . . .	3
<b>2 Extracting phase from defocus : The Transport of Intensity Equation</b>	<b>6</b>
2.1 The phase of propagating light . . . . .	6
2.2 Phase imaging using defocus measurements . . . . .	7
2.3 The Transport of Intensity Equation . . . . .	9
2.4 Solving for phase from the Transport of Intensity Equation . . . . .	10
2.5 Robustness under partial coherence . . . . .	11
<b>3 Phase imaging for photomasks : The Iterative TIE</b>	<b>14</b>
3.1 Through-focus behavior of thin masks . . . . .	14
3.2 Extracting quantitative phase using Transport of Intensity . . . . .	17
3.3 Solver errors for strongly absorbing objects . . . . .	17
3.4 Applying the Iterative TIE . . . . .	19
<b>4 Measuring edge effects using quantitative phase imaging</b>	<b>22</b>
4.1 Experiments on AIMS tool . . . . .	23
4.2 Comparison with thin mask boundary layer simulations . . . . .	24
4.3 Measured edge effects in OMOG vs. ATT-PSM . . . . .	27
4.4 Limitations . . . . .	27
4.5 Conclusions . . . . .	28
<b>5 The TIE with non-uniform illumination</b>	<b>30</b>
5.1 Patterning illumination phase . . . . .	31
5.2 Patterning illumination intensity . . . . .	32
5.3 Recovering phase using patterned illumination . . . . .	33

<b>6 Summary and Future work</b>	<b>39</b>
<b>Bibliography</b>	<b>41</b>

# List of Figures

1.1	Principle of operation of a phase shift mask. The thick MoSi layer has a phase shift of $180^\circ$ as shown in the plot in the middle, where the light through the absorber is out of phase with the light diffracted around the edges. The bottom plot shows the final image, with reduced net intensity in the dark regions. . . . .	2
1.2	Schematic illustrating the difference between attenuating phase shift mask (ATT-PSM) and Opaque MoSI on Silicon (OMOG). ATT-PSM masks are $\pi$ phase shifting at the absorber and hence have a thick absorber stack, causing diffraction at the edges. More efficient attenuating materials allow OMOG masks to have a thinner absorber stack at smaller phase shift and higher absorption, mitigating the diffraction induced phase effects at the edges of features. . . . .	2
1.3	Modeling edge effects with simulation vs. experiment. Rigorous FDTD simulations[5] can be used to estimate the effective complex valued thin mask boundary layers due to edge effects. Here we propose the use of through-focus measurements from an aerial imaging tool (AIMS) to extract the phase at the wafer plane, from which the boundary layer values can be estimated directly. . . . .	3
1.4	Schematic showing an Aerial Imaging and Measurement System (AIMS) tool. The AIMS tool accepts an input mask and images it to the wafer plane with demagnification, similar to a projection printer. The image at the wafer plane is captured on a camera, which allows metrologists to measure the intensity at the wafer plane for a given mask. . . . .	4
2.1	The relative optical path length through a transmitting object at different points across its surface depends on the refractive index contrast with the surrounding media and the object thickness at those points. Phase images can hence give information about the object's structure and shape. . . . .	7
2.2	Iterative phase methods can recover phase from intensity measurements at two or more planes, given the transfer function between the planes. This schematic shows the Gerchberg-Saxton [8] method for recovering phase from intensities measured at two planes of propagation. . . . .	8

2.3	The Transport of Intensity Equation (TIE) can be used to recover phase from closely spaced defocus measurements in an optical microscope. a) Stack of images through-focus for a cheek cell sample. b) The intensity difference about focus is related to the phase by the TIE, which can be inverted to recover the phase profile. The recovered phase in radian shows the optical density of the cell. . . .	8
2.4	The Transport of Intensity equation remains valid for an extended Koehler source which is symmetrical about the optical axis. Contributions to the defocus plane intensity $I_z$ due to source points bisected by the axis cancel out on incoherent addition, maintaining the applicability of the Transport of Intensity for small defocus distance $z$ . . . . .	13
3.1	a) The wafer plane intensity for a pure amplitude object varies quadratically through focus (focus is $z=0$ ). b) Phase effects introduce a linear intensity variation through focus. c) The net effect is a shifted parabola, which is no longer symmetric about $z=0$ . . . . .	15
3.2	Through-focus behavior for a sample pixel close to the phase transition edge is plotted using SPLAT simulation software. a) Without boundary layers (no edge effects) the mask is a pure amplitude object and the intensity varies symmetrically through focus. b) With a quadrature phase boundary layer added at the vertical edge (shown in pink), the through-focus intensity is asymmetric about the focal plane. . . . .	16
3.3	Strongly absorbing isolated contact feature on a clear mask with phase along the vertical edges shows non-zero curl in the Poynting vector near the corners of the feature, which gives rise to artifacts in the recovered phase. The simulation is designed to replicate experiments on an OMOG mask. . . . .	19
3.4	Simulations of a 98% absorbing object with phase near the absorption edges show that the phase recovered in areas of strong absorption tends to have non-physical artifacts when using the regular solver. The through-focus images are simulated in MATLAB and inverted as a Transport of Intensity equation from their $\frac{dI}{dz}$ value at focus. The recovered phase has saddle artifacts due to curl effects, which can be corrected by the iterative solver. . . . .	20
3.5	Schematic showing one iteration of the iterative TIE algorithm. Once the measured through-focus intensity gradient has been solved to recover the phase, the inverse solver is used to get an updated estimate of the gradient, which may not match measurements due to solver artifacts. The residual between the measured and estimated derivatives is solved again as a TIE equation to get the phase residual, which is subtracted from the recovered phase for an improved estimate.	20

4.1	a) The 3D topography of attenuating masks causes diffraction near the feature edges, which shows up as phase edge effects at the wafer plane. b) Thick mask topographical effects can be modeled as polarization-dependent thin mask boundary layers. The boundary layers are complex valued, with real and imaginary parts for an ATT-PSM mask shown in the table.[5]	22
4.2	Aerial Imaging and Measurement System (AIMS) tool captures through-focus intensity images at the wafer plane from which the phase near the edges can be recovered. The mask is clear field OMOG with 2% absorber transmission, the absorbing feature is a 240nm isolated contact.	23
4.3	Phase recovered from experimental through-focus images for an OMOG mask shows errors with the TIE solver, which are mitigated with the help of an iterative method that estimates the error and subtracts it from the phase result in a subsequent iteration step.	24
4.4	Phase recovery of edge effects in an OMOG mask a) Cutlines across the center of the feature show phase peaks at the location of edge effects. The edge effects are quantified as an angle $\times$ width product, which for the TM edge effect gives a value of $900^\circ nm$ . b) Changing the direction of polarization changes the direction of the dominant edge effects. For x-polarized illumination, the dominant edge effects are along the x cutline in the TM direction. For y-polarized illumination, the dominant edge effects are still in the direction of polarization (TM), as seen in the y cutline.	25
4.5	SPLAT thin mask simulations show that the spreading of the mask boundary layer at wafer by the imaging system conserves the angle-width product. The blue and red cutlines correspond to the phase at mask and wafer. Both cutlines show an absorber angle of $10^\circ$ near the center of the block, with the red cutline having spread on going through the imaging system, such that the peak angle measured from the substrate is inversely reduced to preserve the height-width product.	26
4.6	Thin mask simulations with quadrature phase ( $90^\circ$ ) boundary layers fit the phase recovered from experiments with OMOG mask. a) Simulation performed with vertical boundary layers are compared with experiments with x-polarized light. The mask boundary layer is at an angle of $90^\circ$ , with the width chosen to be 10nm ( $900^\circ nm$ ). b) Cutlines comparing wafer plane phase for simulation and experiment. The angle-width product stays conserved for the red line (simulation) from mask to wafer, which agrees with the blue line from experiment, with a corresponding angle-width product of $900^\circ nm$ .	26
4.7	Comparing edge effects in phase shift mask (ATT-PSM) and OMOG for x-polarized light. a) The edge effects are in the direction of the polarization in both cases. b) Overlapping the phase cutlines shows that the ATT-PSM has an absorber angle of $5^\circ$ , corresponding to a real angle of $185^\circ$ , compared to $10^\circ$ for OMOG. The edge effects are about the same height, but the ATT-PSM has twice the spread when compared with OMOG.	27

4.8	Edge effects for two features sizes above and below the resolution limit of the imaging system, for x-polarized illumination. a) A 240nm square has two distinct peaks in the x-cutline, the edge effects for the two vertical edges are resolved in the phase image. b) Shrinking the feature size to below the resolution limit to 120nm makes the peaks indiscernible, a single peak seen in the x-cutline of the recovered phase image. . . . .	28
4.9	The phase sensitivity is limited by the noise in the intensity measurements. A simulation of rms noise in the recovered phase with increasing noise in the intensity shows a linear dependence. The experiments have rms noise of about 0.003; the corresponding phase noise is 0.01radian/pixel, two orders of magnitude smaller than the phase signal due to edge effects. . . . .	29
5.1	Schematic illustrating a patterned illumination, represented as complex field $\sqrt{I_{illu}}e^{i\Phi}$ , interacting with a thin sample, $\sqrt{I}e^{i\phi}$ , and propagating to defocus. . .	30
5.2	Comparison of the transfer functions of the first and second derivative shows that the first derivative provides more signal at lower frequencies, and is hence more robust to low frequency noise in the reconstructed phase. . . . .	32
5.3	Defocus measurements with patterned illumination can be used to recover the phase gradient of a simulated phase object. The figure shows intensity images of a phantom phase object that is numerically propagated to defocus distance $z$ with a plane wave illumination and sinusoid illumination pattern respectively. .	34
5.4	The two defocus intensity measurements with the patterned illumination and the plane wave illumination can be combined to extract the refraction term, i.e. the product of the phase gradient and illumination gradient, which is demodulated in a further step. . . . .	34
5.5	Schematic showing the demodulation of the refraction term, the product $\nabla I \cdot \nabla \phi$ , using two stripe patterns shifted by a quarter period. a) The product $\nabla I \cdot \nabla \phi$ is multiplied by the sign of the illumination gradient, which makes the divisor of the phase gradient purely positive, albeit still with zeros. b) Performing the same procedure for the pattern shifted by quarter of the period shifts the position of the zeros. c) Addition of the resulting patterns has no zeros in the divisor, which can be directly divided to recover the phase gradient in the direction normal to the stripes, $\nabla_y \phi$ . . . . .	35
5.6	The phase gradients extracted from structured illumination in either direction can be combined to reconstruct the two dimensional phase, in this case a phantom phase object. . . . .	36
5.7	Schematic showing the experimental setup for the recovery of the first order phase gradient using structured illumination. A binary deformable mirror device is used to structure the illumination, which is demagnified and focused onto the cheek cell sample using a 40x objective. The resultant field is magnified with another objective and imaged onto the camera, which is at an effective defocus plane of the sample. . . . .	38

5.8	The phase gradients extracted from structured illumination in orthogonal directions $x$ and $y$ can be combined to reconstruct the two dimensional phase for a cheek cell. . . . .	38
-----	--	----

## **Acknowledgments**

Deeply indebted to Professors Laura Waller and Andy Neureuther for providing the vision leading to the ideas presented in this work. Many thanks also to Martin Sczyrba, Brid Connolly and others at AMTC, Dresden for support and collaboration on the experimental results. Final word of gratitude to the body of thinkers and doers that have kept the wheels of inquiry and invention moving along, for we can see far only because we stand on the shoulders of giants.

# Chapter 1

## Introduction

Optical lithography is the process of imaging patterns from a pre-inscribed mask to a photosensitive resist coating on wafer, etching which transcribes the patterns onto the wafer. Diffraction effects at mask edges influence the phase of the electromagnetic field and are of concern to lithographers, as optical phase defines the through-focus intensity behavior at the wafer plane, impacting the process window during layout and design. Additionally, printed feature sizes in modern chip manufacturing are at the tens of nanometers scale; hence undesired phase at the thick edges of absorber stacks in photomasks can have a major impact on manufacturability and throughput, especially as scaling continues to reduce node sizes and tighten process windows. We aim to measure and model these edge effects to better enable mask designers and OPC engineers to understand their behavior and mitigate undesirable consequences.

### 1.1 Electromagnetic edge effects in photomasks

Traditional chrome masks are purely absorbing with no designed phase shifts; the absorber however diffracts light around feature edges causing stray light to fall onto the dark regions. As feature sizes have reduced with progressive scaling, the process has grown more sensitive to the diffracted light in the dark areas, and absorbing masks have been mostly replaced with phase shift masks around the 65 nm node size. Attenuating phase shift masks let through a small fraction of out-of-phase light through the absorber, which destructively interferes with diffracted light to print sharper features on the resist, as shown in figure 1.1.

PSMs however have their own problems - the phase shifts are implemented by increasing the thickness of the absorber stack, increasing the severity of diffraction at feature boundaries. Hence, despite the improved contrast in the intensity images, the phase of the light near feature boundaries has undesirable variations due to edge effects. As the phase of the electromagnetic field impacts through-focus behavior of intensity, smaller nodes which have a smaller depth of focus during printing are more susceptible to edge effects. More recently, OMOG (Opaque MoSi on Glass) masks have replaced phase shift masks at 45nm and 22nm

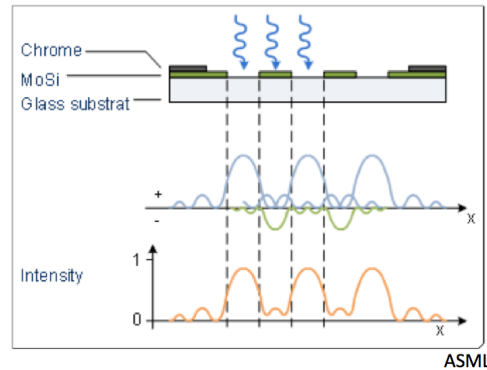


Figure 1.1: Principle of operation of a phase shift mask. The thick MoSi layer has a phase shift of  $180^\circ$  as shown in the plot in the middle, where the light through the absorber is out of phase with the light diffracted around the edges. The bottom plot shows the final image, with reduced net intensity in the dark regions.

nodes[1], where the phase shift has been abandoned in favor of thinner, better attenuating absorber materials, as shown in the schematic in figure 1.2.

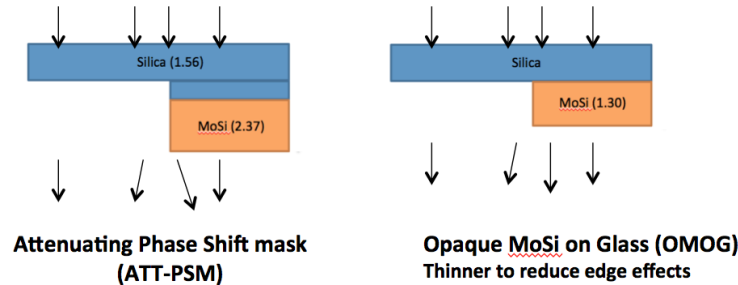


Figure 1.2: Schematic illustrating the difference between attenuating phase shift mask (ATT-PSM) and Opaque MoSi on Silicon (OMOG). ATT-PSM masks are  $\pi$  phase shifting at the absorber and hence have a thick absorber stack, causing diffraction at the edges. More efficient attenuating materials allow OMOG masks to have a thinner absorber stack at smaller phase shift and higher absorption, mitigating the diffraction induced phase effects at the edges of features.

The diffraction around thick edges is a significant effect, as suggested by the transition to a thinner absorber in OMOG, which mitigates phase effects at the edges but doesn't wholly eliminate them. The ability to measure these phase effects would enable mask designers and proximity correction engineers to compensate for them during mask layout, or process engineers to design the process window while accounting for edge effects.

## 1.2 Characterizing edge effects

### Full wave simulations

Thick mask edge effects modify the best focus and also the through-focus behavior of the wafer plane images, and hence need to be modeled. Thin mask boundary layer models have been proposed[2, 3, 4] that can approximate diffraction along thick edges as effective boundary layers in simulations. Miller et al.[5] used FDTD simulations on the full 3D geometry of the mask to show that complex valued 2D boundary layers can approximate 3D effects, as shown in Fig 1.3 for an Opaque MoSi on Silica (OMOG) mask. The boundary layers are found to be complex valued, the real part of the boundary layer results in a shifted edge position, and the imaginary part contributing to the phase at the wafer plane. The edge effects are primarily in the direction of the illumination polarization, the transverse magnetic (TM) component in polarization direction being about four times as pronounced as the transverse electric (TE) component [5].

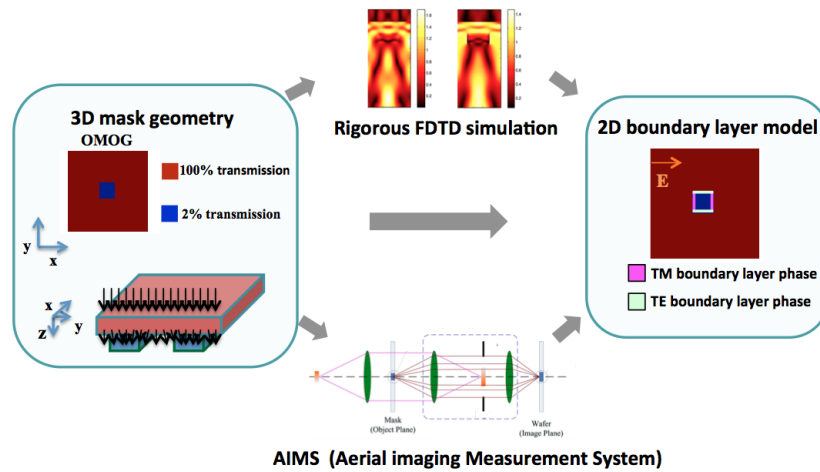


Figure 1.3: Modeling edge effects with simulation vs. experiment. Rigorous FDTD simulations[5] can be used to estimate the effective complex valued thin mask boundary layers due to edge effects. Here we propose the use of through-focus measurements from an aerial imaging tool (AIMS) to extract the phase at the wafer plane, from which the boundary layer values can be estimated directly.

### Aerial image measurements

Despite being a workhorse for predicting electromagnetic effects, full wave simulations rely on forward models of the mask imaging process and hence have to make certain general assumptions about the imaging system, besides being computationally intensive for large

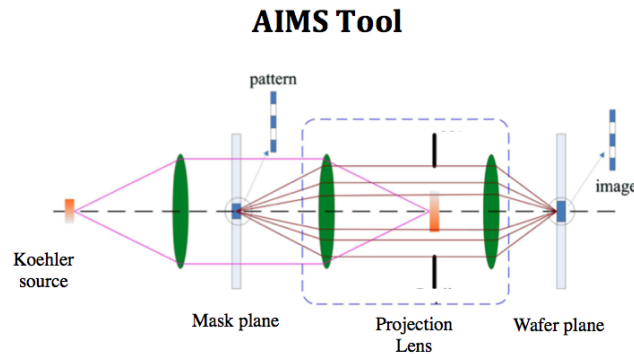


Figure 1.4: Schematic showing an Aerial Imaging and Measurement System (AIMS) tool. The AIMS tool accepts an input mask and images it to the wafer plane with demagnification, similar to a projection printer. The image at the wafer plane is captured on a camera, which allows metrologists to measure the intensity at the wafer plane for a given mask.

intricate masks. Characterizing edge effects by inverting measurements from the imaging system, on the other hand, enables fast and direct computation of the system-specific phase effects at the wafer plane.

The experimental approach adopted here uses measurements from an aerial imaging tool to characterize the electromagnetic edge effects from intensity measurements at the wafer. As the through-focus intensity behavior at the image plane is dependent on the electric field phase at the wafer plane, the through focus behavior can be inverted to extract the phase from measurements, and subsequently quantify electromagnetic diffraction at feature edges.

Figure 1.4 shows the schematic of an Aerial Imaging and Measurement System (AIMS) tool, used for studying the fields at the wafer plane for a mask during inspection and metrology. The system replicates a projection printer in most aspects, with a camera at the back end replacing the silicon wafer. The field at the wafer plane is magnified back onto the camera, and enables inspection of the intensity that would have been printed on the silicon wafer. Since the AIMS tool has an adjustable focus to characterize the through-focus behavior of the wafer plane intensity, it is hence a suitable tool for quantifying the wafer plane phase using defocus measurements.

In following chapters we apply the Transport of Intensity method on through-focus intensity images from an aerial imaging tool for an isolated contact feature. We discover that the conventional Fourier domain methods to solve phase from intensity derivative measurements produce artifacts in the presence of strong absorption and edge effects. These artifacts are fixed with a gradient descent style iterative solution, with the final images showing quantitative evidence of polarization dependent edge effects in the recovered phase. Chapter 2 describes the transport of intensity equation in greater detail, and chapter 3 describes the artifacts that arise in the presence of strong absorption and the iterative method which can

remove them. Chapter 4 applies the iterative algorithm to identify and quantify edge effects for a feature at the resolution limit, and corroborates the values measured for ATT-PSM and OMOG masks with those from rigorous simulations in literature. Chapter 5 generalizes the defocus based imaging methodology to more general illumination schemes, demonstrating a technique of recovering phase from intensity measurements at a single defocus plane using multiple illumination patterns.

## Chapter 2

# Extracting phase from defocus : The Transport of Intensity Equation

### 2.1 The phase of propagating light

Light transport is modeled as wave propagation by the Maxwell's equations, which solve for the complex valued electric and magnetic field as light travels through a dielectric medium. The intensity of the wave is a bilinear function of the field amplitude, and can be directly measured by a photon flux detecting device such as a CMOS camera. Optical phase, a wave property of the propagating light, cannot be directly measured due to the rapidity of the wave oscillations (on the order of THz for visible light). Relative phase shifts, however, are often of interest for imaging application since they correspond directly to the optical path length of a transmissive sample, as shown in Fig. 2.1. In thick photomasks, for instance, deviations from the designed phase are an indicator of topographical diffraction effects that modify the optical path length of the imaged light. Biologists and doctors have found tremendous utility in examining quantitative phase images of microscopic samples and X-Ray scans of the human body respectively, and lithographers could do the same.

The propagation of coherent light depends uniquely on both its amplitude and phase at a given plane. In lithographic setups, where a projection printer acts to image a transmissive mask onto the wafer substrate, variations in the phase of the mask will change the through-focus behavior of optical intensity, and hence put restrictions on the defocus tolerance of the system. Quantitative phase measurements that invert the phase from propagated intensity can be used to image phase defects, measure uniformity across the mask, and help tighten the process window by correcting for stray phase effects using proximity correction methods. The following sections introduce the Transport of Intensity phase imaging method used in this work for extracting phase from defocus intensity, delving into some of its properties and nuances.

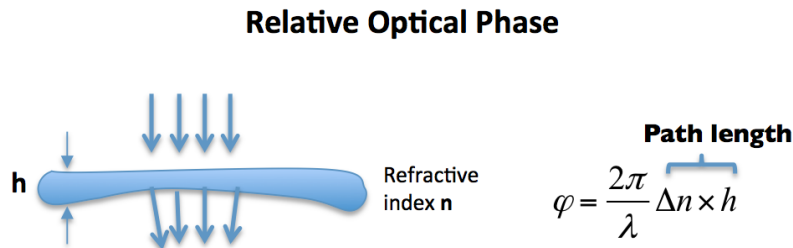


Figure 2.1: The relative optical path length through a transmitting object at different points across its surface depends on the refractive index contrast with the surrounding media and the object thickness at those points. Phase images can hence give information about the object's structure and shape.

## 2.2 Phase imaging using defocus measurements

Interferometric methods have typically been used for looking at phase variations in coherent light beams, and reveal the phase of an optical beam by comparing with a coherent reference. Due to strict conditions on coherence and alignment of the reference beam, however, these methods are limited in scope. Additionally the need for an extra reference beam makes them impractical for use with existing imaging systems without major hardware modifications, especially in the EUV and X-Ray regimes. Hence defocus based phase imaging methods are preferred in such cases.

In principle, phase recovery from intensity measurements can be performed with any transfer function which couples phase information of the complex valued field into intensity measurements. Iterative methods that use the Fourier transform as the transfer function, iterate between an intensity measurement and the corresponding intensity of the Fourier transform, imposing the measured intensity at each plane until the solution converges to a stable phase value[6, 7] at given intensities. A similar methodology can be used in the fractional Fourier domain, which is equivalent to free space propagation for an electromagnetic wave, or to defocusing for an imaging system. A typical iterative scheme for phase estimation is shown in Fig. 2.2.

Iterative methods are computationally intensive, and convergence properties are object and transfer function dependent. Although applicable to virtually any transfer function, the convergence to a solution and corresponding error bounds are difficult to predict in purely iterative methods, especially when the initial guess for the phase is arbitrary.

Deterministic phase retrieval methods, on the other hand, rely on an invertible transfer function from which the phase is directly solved, enabling real-time recovery of phase. The Transport of Intensity is one such deterministic method, which recovers phase starting from a small defocus approximation that linearizes the dependence of defocused intensity on phase.

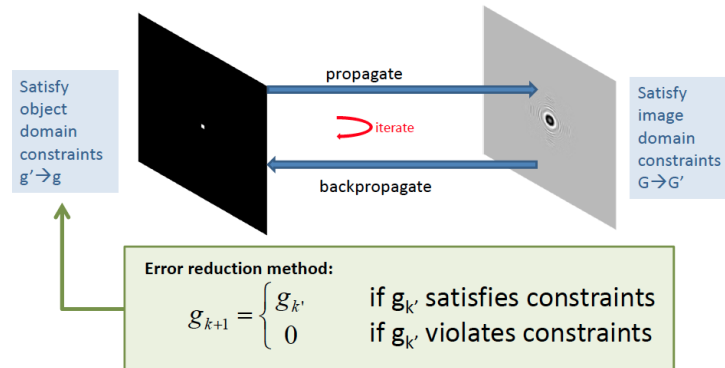


Figure 2.2: Iterative phase methods can recover phase from intensity measurements at two or more planes, given the transfer function between the planes. This schematic shows the Gerchberg-Saxton [8] method for recovering phase from intensities measured at two planes of propagation.

A stack of through focus intensity images, from a microscope in this case, can then be inverted to recover the phase as shown in Fig 2.3

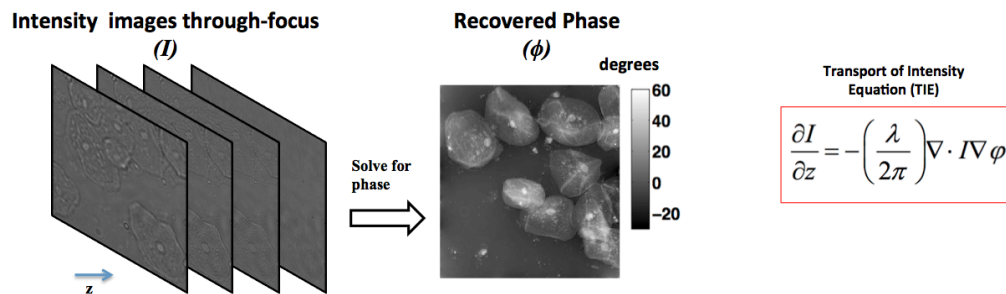


Figure 2.3: The Transport of Intensity Equation (TIE) can be used to recover phase from closely spaced defocus measurements in an optical microscope. a) Stack of images through-focus for a cheek cell sample. b) The intensity difference about focus is related to the phase by the TIE, which can be inverted to recover the phase profile. The recovered phase in radian shows the optical density of the cell.

The Transport of Intensity Equation (TIE) models the intensity difference on propagation as a second order differential equation in the wavefront intensity and phase, which is solved for the phase starting from intensity measurements. [9, 10]. The equation assumes a paraxial approximation, which is most valid for small defocus distances, as elaborated in section 2.5. The advantage of the method is in the fast, direct recovery of phase from defocus measurements and the simplicity of the underlying experimental apparatus. Most imaging

systems, including projection printers used in wafer printing, come with a focusing knob, enabling TIE based phase imaging with existing hardware.

## 2.3 The Transport of Intensity Equation

In this section we derive the Transport of Intensity equation (TIE) starting from conservation principles for optical power flow. Most generally, the continuity equation describes a conserved vector field  $\vec{D}$  in a N dimensional space as

$$\vec{\nabla}_{1,2,3..N} \cdot \vec{D} = 0$$

where  $\vec{\nabla}_{1,2..N} = \{\partial x_1, \partial x_2, \dots, \partial x_N\}$  are the partial derivatives. In the case of physical quantities conserved in space- time the equation is alternatively written as

$$\vec{\nabla}_{x,y,z} \cdot \vec{D} = -\frac{\partial D}{\partial t}$$

Physical systems are often understood by modeling the dynamics of conserved quantities, and hence the continuity equation arises in various disciplines, such as fluid mechanics (Navier-Stokes), heat flow, quantum mechanics (probability current) and electromagnetism (electric current). Propagating light in source-free space can be described as electromagnetic oscillations; the corresponding harmonic electric field has a stationary solution in three dimensional space (x,y,z) given by

$$E = \sqrt{I(x, y, z)} e^{i\phi(x,y,z)}$$

In this case the conserved vector field is the power vector, also known as the Poynting vector from the Poynting theorem [11]

$$\vec{P} = I \vec{\nabla}_{x,y,z} \phi$$

where the  $\vec{\nabla}_{x,y,z}$  operator is the three dimensional gradient acting on the electric field phase  $\phi$ . The magnitude of the Poynting vector is the intensity  $I(x,y,z)$ . and the direction is normal to the wavefront, given by the Huygen's principle as  $\vec{\nabla} \phi$ . Hence the power conservation equation for propagating light in free space is given by the continuity equation for the Poynting vector,

$$\begin{aligned} \vec{\nabla}_{x,y,z} \cdot \vec{P} &= 0 \\ \Rightarrow \vec{\nabla}_{xyz} \cdot I \vec{\nabla}_{xyz} \phi &= 0 \end{aligned}$$

A paraxial approximation assumes most of the wave energy to be traveling close to the axis of propagation, say z, in which case the wave is almost a plane wave in z,

$$E = \sqrt{I(x, y, z)} e^{i(kz + \phi(x,y))}$$

where  $k = \frac{2\pi}{\lambda}$  is the propagation constant, and we make the approximation that  $k_z \approx k$ . The continuity equation then becomes [12]

$$\vec{\nabla}_{xyz} \cdot I \vec{\nabla}_{xyz} \{kz + \phi(x, y)\} = 0$$

$$\vec{\nabla}_{\perp} \cdot I \vec{\nabla}_{\perp} \phi(x, y) = -k \frac{\partial I}{\partial z} \quad (2.1)$$

where  $\nabla_{\perp} = \nabla_{x,y}$  is the two dimensional gradient operator, represented henceforth as  $\nabla = \nabla_{\perp}$  for compactness. Equation 2.1 is the Transport of Intensity Equation (TIE), which relates the through-focus ( $z$  axis) intensity gradient to the two dimensional ( $x$ - $y$ ) intensity and phase distribution. The equation is a useful approximation of paraxial light propagation as it can be inverted to recover the phase using intensity measurements in the axial direction.

A typical result is shown in Figure 2.3 [13]. Intensity measurements at different defocus planes of a microscope are used to estimate  $dI/dz$  at the focal plane for a transparent biological sample with phase variations. Equation 2.1 can then be inverted to solve for phase  $\phi$ , as described in the following section.

## 2.4 Solving for phase from the Transport of Intensity Equation

The TIE is typically solved [9] by converting the divergence of the Poynting vector,  $\vec{\nabla} \cdot I \vec{\nabla} \phi$ , into a double derivative using the following substitution,

$$I \vec{\nabla} \phi = \vec{\nabla} \psi \quad (2.2)$$

in Eqn. 2.1, giving,

$$\frac{dI}{dz} = -\frac{\lambda}{2\pi} \nabla^2 \psi \quad (2.3)$$

where  $\psi$  is an auxiliary variable. Equation 2.3 is a Poisson equation, and can be integrated in the Fourier domain [14, 15], as follows,

$$\psi = \mathcal{F}^{-1} \left[ -\frac{2\pi}{\lambda} \frac{\mathcal{F} \left( \frac{dI}{dz} \right)}{-4\pi^2 f^2 + \epsilon} \right] \quad (2.4)$$

where  $f$  is the spatial frequency variable,  $\epsilon$  is a regularization parameter, and  $\mathcal{F}$  represents a Fourier transform. The regularization avoids division by zero frequency, but degrades the reconstruction fidelity of low spatial frequencies. Periodic boundary conditions are implied due to the periodic property of the discrete Fourier transform, and a mirror flipping method is used to eliminate discontinuities at the boundary[16].

For a pure phase object, the intensity is constant in-plane,  $I(x, y) = I_0$ , and the phase is simply  $\phi = \psi/I_0$ . More generally though, once  $\psi$  is known, another Poisson equation needs to be solved to obtain the phase  $\phi$ , as follows,

$$\begin{aligned} I\vec{\nabla}\phi &= \vec{\nabla}\psi \\ \Rightarrow \vec{\nabla} \cdot \frac{\vec{\nabla}\psi}{I} &= \nabla^2\phi \end{aligned} \quad (2.5)$$

which is then similarly inverted by a Poisson solver to recover the final phase  $\phi(x, y)$ .

Inaccuracies in the inverted phase,  $\phi$  arise due to approximations in estimating  $dI/dz$  from measurements, or due to the Poisson solver which is noise and regularization sensitive. Methods such as using more through-focus images[17] or estimating the derivative in the Fourier domain [13] have been shown to improve the derivative estimation as well as noise tolerance of the solution.

The TIE has been commonly used for imaging phase in other applications such as optical microscopy[18], electron microscopy[19] and X-Ray imaging[20, 21]. As demonstrated in the next section, it is fairly robust under partially coherent illumination[22, 23] which makes it particularly suitable for looking at phase also in lithography.

## 2.5 Robustness under partial coherence

Applicability under varying degrees of coherence is an important requirement for any phase imaging method that is intended for lithographic applications, as sources used in projection printers tend to be partially coherent for maximizing resolution. In this section we derive the TIE from a Taylor series approximation of defocus, and show that the TIE stays valid for partially coherent illumination as long as the source is symmetric.

### The Transport of Intensity as a small defocus approximation

The TIE of equation 2.1 can also be obtained as a first order approximation of defocused electric field. Defocus can be modeled as convolution with the paraxial point spread function (PSF),  $h_z(x, y)$ ,

$$h_z(x, y) = \frac{e^{ikz}}{i\lambda z} \exp\left(ik \frac{x^2 + y^2}{2z}\right)$$

where  $\lambda$  is the wavelength, and  $k = \frac{2\pi}{\lambda}$  is the spatial frequency. Starting from an electric field  $E_0 = \sqrt{I}e^{i\phi}$ , the field at a defocus distance of  $z$  is given as a convolution by the PSF,  $h_z(x, y)$ ,

$$E_z = E_0(x, y) \otimes \exp\left(ik \frac{x^2 + y^2}{2z}\right)$$

In the Fourier domain,  $x \rightarrow u$  and  $y \rightarrow v$ , the convolution becomes a product,

$$\mathcal{E}_z(u, v) = \mathcal{E}_0(u, v) \times \exp(-i\pi\lambda z(u^2 + v^2))$$

The exponential can be Taylor expanded as a polynomial,

$$\mathcal{E}_z(u, v) = \mathcal{E}_0(u, v) \times [1 - i\pi\lambda z(u^2 + v^2) + \pi\lambda^2 z^2(u^2 + v^2)^2 + O(\lambda^3 z^3) \dots]$$

On inverse Fourier transforming, the property  $u^2 + v^2 \rightarrow -\nabla^2/4\pi^2$  can be applied, and the defocus field in the spatial domain is obtained as,

$$E_z(x, y) = [E_0(x, y) + i\frac{\lambda z}{4\pi}\nabla^2 E_0 + O(\lambda^2 z^2)]$$

The intensity is bilinear in electric field  $E$ , and hence we can write

$$I_z(x, y) = E_z E_z^* = I(x, y) - \frac{\lambda z}{2\pi}\nabla \cdot I\nabla\phi + O(\lambda^2 z^2) + \dots \quad (2.6)$$

where the substitution  $E_0(x, y) = \sqrt{I}e^{i\phi}$  has been used. A finite difference about  $z=0$  will remove all terms with an even exponent in  $z$ , including the quadratic  $z^2$  terms, yielding the TIE of equation 2.1

$$I_z(x, y) - I_{-z}(x, y) = -\frac{\lambda(2z)}{2\pi}\nabla \cdot I\nabla\phi + O(\lambda^3 z^3) \quad (2.7)$$

Hence the error term is of the order of  $z^3$  (with third order derivatives and higher), strengthening the case for dropping the higher order terms within the small defocus regime. The finite difference can be approximated as a derivative to obtain the more familiar form of the Transport of Intensity as a first order derivative,

$$\frac{dI}{dz} \approx \frac{I_z(x, y) - I_{-z}(x, y)}{2z} = -\frac{1}{k}\nabla \cdot I\nabla\phi \quad (2.8)$$

## Validity of the TIE for an extended source

In the presence of an off-axis source at an angle  $\alpha$ , the equation 2.6 gets an extra term proportional to the gradient of object intensity,  $\nabla I$ , and the illumination angle  $\alpha$ ,

$$I_z(x, y) = I - \frac{\lambda z}{2\pi}\{\nabla \cdot I\nabla\phi + \alpha\nabla I\} + O(\lambda^2 z^2) + O(\lambda^2 \alpha^2 z^2) + \dots \quad (2.9)$$

with extra higher order shift terms of  $O((\lambda\alpha z)^n)$  also appearing due to the off-axis illumination, as also discussed in section 5.1. An extended source can be modeled as an incoherent sum of intensity over  $\alpha_i$ , as shown in figure 2.4, and the defocus intensity becomes,

$$I_z(x, y) = I - \frac{\lambda z}{2\pi}\left\{\nabla \cdot I\nabla\phi + \frac{\sum_i \alpha_i \nabla I}{S}\right\} + O(\lambda^2 z^2) + O(\lambda^2 z^2 \sum_i \alpha_i^2) + \dots \quad (2.10)$$

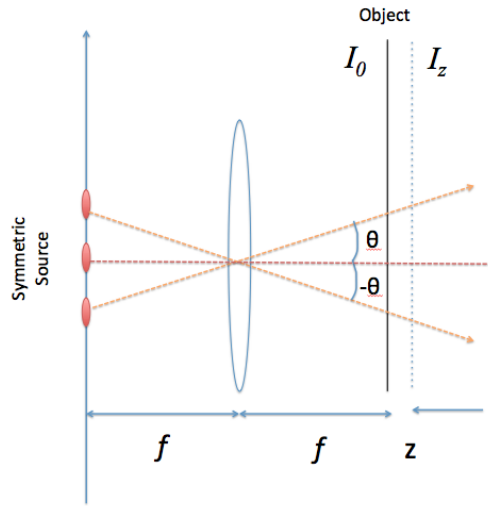


Figure 2.4: The Transport of Intensity equation remains valid for an extended Koehler source which is symmetrical about the optical axis. Contributions to the defocus plane intensity  $I_z$  due to source points bisected by the axis cancel out on incoherent addition, maintaining the applicability of the Transport of Intensity for small defocus distance  $z$ .

where  $S$  is the total number of points being summed over. Now in the presence of symmetry in the source,  $\sum_i \alpha_i^n$  is zero for odd values of  $n$  as points at  $\pm\alpha$  add to give a zero sum. Hence a symmetric extended source will remove error terms of the type  $O((\lambda z \alpha)^n)$  for odd  $n$ , and a symmetric finite difference about  $z = 0$  will eliminate terms of the form  $O((\lambda z \alpha)^n)$  for even  $n$ , recovering the finite difference equation 2.7 for a coherent source,

$$I_z(x, y) - I_{-z}(x, y) = -\frac{\lambda(2z)}{2\pi} \nabla \cdot I \nabla \phi + O(\lambda^3 z^3) \quad (2.11)$$

and subsequently the Transport of Intensity equation as a partial derivative. Comparing equations 2.7 and 2.11 shows that the error for a symmetric extended source is invariant of the incoherence parameter  $\alpha$ . Sources used in lithography are generally extended sources with symmetry about the center, examples being extended circular sources, dipole sources, and quadrupole sources. The analysis here does not account for finite numerical aperture of the imaging system, assuming that the features are low frequency and hence far from the bandlimit of the system. Nevertheless it goes to show that the Transport of Intensity is robust under an extension of the point source while maintaining symmetry[10], and hence a suitable phase imaging method for lithographic systems.

## Chapter 3

# Phase imaging for photomasks : The Iterative TIE

We have seen in chapter 2 that the Transport of Intensity equation(TIE) can be used to recover the phase from a stack of through-focus aerial images [24]. In this chapter we develop a modified version of the TIE to remove artifacts due to strong absorption in the attenuating masks under test.

### 3.1 Through-focus behavior of thin masks

A thin mask can be modeled as a two dimensional complex transmittance function with a net amplitude and phase at each point on its surface. When imaged to the wafer plane, the at-focus intensity image of the mask shows only the amplitude profile, the phase being invisible at focus. The mask phase does however influence the intensity at defocus planes; hence through-focus images can be typically used to investigate phase effects at the wafer.

This section describes the through-focus behavior of mask amplitude and phase. For small defocus (less than the Rayleigh defocus distance), pure amplitude objects will vary symmetrically through focus at every point on the two dimensional plane. More specifically, this variation is quadratic, as shown in figure 3.1a. For a 2D mask in the  $x - y$  plane,  $\psi(x, y) = \sqrt{I(x, y)}e^{i\phi(x, y)}$ , the through-focus variation in the third dimension,  $z$ , can be written as [25]

$$I(x, y, z) = Q(x, y)z^2 + I(x, y, 0) \quad (3.1)$$

where  $I(x, y, 0)$  is the intensity at focus( $z = 0$ ), and  $Q(x, y)$  depends on the amplitude derivatives.  $I(x, y, z)$  is thus a parabola in  $z$  which is symmetric about  $z = 0$ . In simpler terms, intensity images at equal and opposite defocus distances are identical for an amplitude object. Phase variations across the thin mask break this symmetry by adding a linear term to the through-focus variation, as also derived in section 2.5,

$$I(x, y, z) = Q(x, y)z^2 + L(x, y)z + I(x, y, 0) \quad (3.2)$$

where  $L(x, y)$  is the linear coefficient (figure 3.3b) and depends on the phase gradient at the mask [26]

$$L(x, y) = -\frac{\lambda}{2\pi} \vec{\nabla}_{\perp} \cdot I(x, y, 0) \vec{\nabla}_{\perp} \phi(x, y) \quad (3.3)$$

$\lambda$  is the wavelength of light used, and  $\vec{\nabla}_{\perp}$  refers to the lateral gradient. The phase gradient dependence of the through-focus intensity is essentially a power flow relation, where  $\vec{\nabla} \phi$  is the direction of power propagation, which makes  $I \vec{\nabla}_{\perp} \phi$  the lateral Poynting vector, whose divergence determines the linear change of  $I(x, y, z)$  with respect to  $z$ .

Equation 3.2 says that through-focus behavior is a laterally shifted parabola, which is no longer symmetric about the  $z = 0$  focal point. Figure 3.1c plots the through-focus behavior modeled by eqn. 3.2. If the linear term  $L(x, y)$  can be extracted from through-focus images, then the phase contributions from the mask at the wafer plane can be quantified by solving eqn. 3.3 for  $\phi$ .

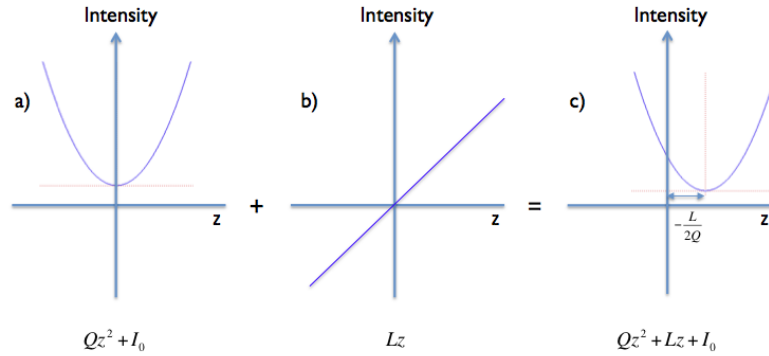


Figure 3.1: a) The wafer plane intensity for a pure amplitude object varies quadratically through focus (focus is  $z=0$ ). b) Phase effects introduce a linear intensity variation through focus. c) The net effect is a shifted parabola, which is no longer symmetric about  $z=0$ .

## Simulation

Simulations in an aerial image simulator (SPLAT<sup>1</sup>) can be used to generate wafer plane images for a test mask and investigate the effect of quadrature phase boundary layers on the through-focus intensity. SPLAT is a 2D projection printing simulator based on Hopkins theory of partially coherent imaging. The example mask used is an attenuating phase shift

<sup>1</sup><http://cuervo.eecs.berkeley.edu/Volcano/>

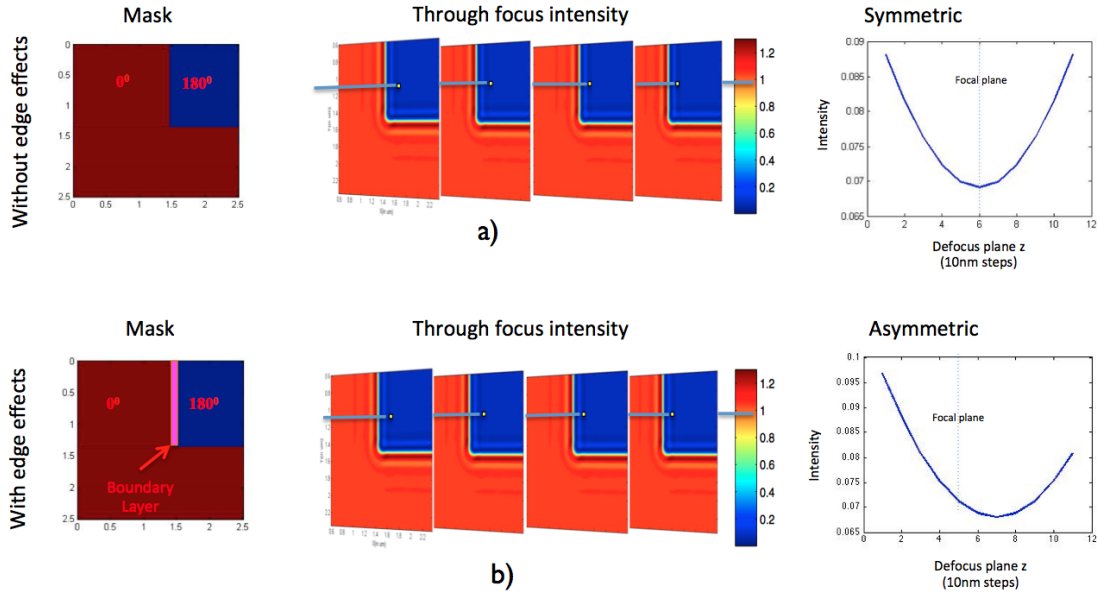


Figure 3.2: Through-focus behavior for a sample pixel close to the phase transition edge is plotted using SPLAT simulation software. a) Without boundary layers (no edge effects) the mask is a pure amplitude object and the intensity varies symmetrically through focus. b) With a quadrature phase boundary layer added at the vertical edge (shown in pink), the through-focus intensity is asymmetric about the focal plane.

mask with a 6% transmittance,  $180^\circ$  phase shift region on a zero phase clear background, as shown in figure 3.2a. The simulations are at deep UV (193nm) wavelength and incoherence parameter  $\sigma = 0.3$ .

The mask in figure 3.2a can be thought of as a pure amplitude object, with the  $\pi$  phase acting as an equivalent negative amplitude. A stack of through-focus images is generated in SPLAT for this mask with the above parameters. As described in the previous section, in the absence of quadrature boundary layers the mask is a pure amplitude object and the through-focus intensity is seen to vary quadratically through focus within the Rayleigh defocus limit. Intensity images on either sides of focus are identical. Hence, for every pixel on the mask, a plot of the intensity through-focus returns a parabola centered about the focal plane (fig. 3.2a), though the width and curvature of the parabola may change with position.

After adding a 20nm wide quadrature phase boundary layer (fig. 3.2b) on the attenuating region at the vertical edge and analyzing the image stack generated by SPLAT, the through-focus intensity obtained for a pixel close to the edge is no longer symmetric. As suggested in eqn. 3.2, the quadrature phase edge creates a phase gradient that adds a linear component to the through-focus behavior. The resultant variation is a laterally shifted parabola which is no longer symmetric about the focal plane. This asymmetry through focus is utilized by

the Transport of Intensity equation to solve for the quantitative phase on the mask using intensity differences about focus, as described next.

## 3.2 Extracting quantitative phase using Transport of Intensity

The Transport of Intensity Equation (TIE) is a propagation based phase imaging technique that utilizes two images on either side of the focal plane to recover the phase at focus, as described earlier in chapter 2. The linear component of through-focus intensity variation is directly related to the phase gradient as shown in eqn. 3.3. For two intensity images at  $z = z_1$  and  $z = -z_1$ , the difference image from equation 3.2 gets rid of the quadratic and constant terms, yielding only the linear term -

$$I(x, y, z_0) - I(x, y, -z_0) = -\frac{\lambda}{2\pi} 2z_0 L(x, y) \quad (3.4)$$

which becomes the more familiar form of the TIE [10] on substituting the value of  $L(x, y)$  from equation 3.3, and recognizing the finite difference approximation for the derivative,

$$\frac{dI}{dz} \approx \frac{I(x, y, z_0) - I(x, y, -z_0)}{2z_0} = -\frac{\lambda}{2\pi} \vec{\nabla}_\perp \cdot I(x, y, 0) \vec{\nabla}_\perp \phi(x, y) \quad (3.5)$$

which can be directly compared with eqns. 2.1 and 2.8, and solved numerically using a Poisson solver as described in section 2.4. Although the method has been used for phase imaging of various samples, such as biological and medical specimen, magnetic materials etc., the unusual amount of absorption present in photomasks causes new artifacts which need to be understood and corrected for, as elucidated in the next section.

## 3.3 Solver errors for strongly absorbing objects

In the presence of strong absorption at the sample, such as in a photomask, diffraction at sharp corners causes a rotational in the in-plane power flow at the sample. The TIE is insensitive to curl in the power flow, and hence gives an erroneous phase result. Here we develop a computational method that iteratively estimates the error due to the missing curl in the solver, and updates the estimated phase giving a much improved result.

It has been noted[27, 28, 12] that the substitution used in equation 2.2 makes an implicit assumption that the Poynting vector  $I\vec{\nabla}\phi$  can be expressed as the gradient of a scalar field, i.e. it is curl free. More generally, however, the Poynting vector can be written as

$$I\vec{\nabla}\phi = \vec{\nabla}\psi + \vec{\nabla} \times \vec{A} \quad (3.6)$$

Since the Transport of Intensity describes the divergence of the Poynting vector,  $\vec{\nabla} \cdot I\vec{\nabla}\phi = \nabla^2\psi$ , the first Poisson equation solved for in eqn. 2.4 accurately solves for the

scalar field  $\psi$ . In the presence of a curl component in the Poynting vector, equation 2.5 has an extra curl term,

$$\vec{\nabla} \cdot \frac{\vec{\nabla}\psi}{I} + \vec{\nabla} \cdot \frac{\vec{\nabla} \times \vec{A}}{I} = \nabla^2\phi \quad (3.7)$$

$$\nabla^2\phi_{TIE} + \nabla^2\phi_{residual} = \nabla^2\phi \quad (3.8)$$

$\phi_{TIE}$  is the phase solved for by the TIE solver, and  $\phi_{residual}$  is the residual error due to the curl component of the in-plane power vector. The missing residual component in the phase recovered by the TIE manifests as non-physical artifacts, as seen in figure 3.4.

### Mitigating curl artifacts : The Iterative TIE

An iterative procedure can be used to estimate the residual and correct the artifacts in the phase recovered by the TIE. The residual phase can be recovered to some extent by calculating the residual  $dI/dz$  due to the solved phase,  $\phi_{TIE}$ ,

$$\left. \frac{dI}{dz} \right|_{residual} = \left. \frac{dI}{dz} \right|_{measured} - \left[ \frac{-1}{k} \nabla I \cdot \nabla \phi_{TIE} \right]$$

and estimating the corresponding residual phase with another iteration of the TIE solver on the following equation,

$$-k \left. \frac{dI}{dz} \right|_{residual} = \nabla I \cdot \nabla \phi_{residual}$$

solving which gives an estimate of  $\phi_{residual}$ . The final phase is obtained by plugging the estimated residual into eqn. 3.8 for an improved phase result.

A visualization of the real phase residual and the estimated phase residual from the iterative step is shown for an example mask in figures 3.4 and 3.5 respectively. The estimated residual is quite similar to the actual residual but not exactly the same; nevertheless the updated phase result compares much better with the real phase than the initial solution. Further iterations improve the estimate of the phase residual, the first one being the most significant. The simulations shown in the figures are described in greater detail in the next section.

For what kind of objects can we expect there to be considerable errors due to the neglected curl? For the Poynting vector to have an error inducing curl component, the following condition has to be met

$$\vec{\nabla} \times I \vec{\nabla} \phi = \vec{\nabla} \times \vec{\nabla} \times \vec{A} \neq 0$$

which is reduced using the expansion for the curl of a product,

$$\Rightarrow \vec{\nabla} I \times \vec{\nabla} \phi \neq 0 \quad (3.9)$$

The curl induced error is object dependent, and exists only if the absorption and phase of the sample have gradients in different directions. Objects such as biological samples have

small absorption for which  $\vec{\nabla} I$  and hence equation 3.9 is close to zero, the curl induced error thus being insignificant, which is also why these kinds of effects have not been explored much previously. In lithography, however, masks often have high absorption, which causes the curl term to be non-zero near sharp corners. The errors thus caused can be mitigated by using the iterative solver, described next.

### 3.4 Applying the Iterative TIE

Lithographic masks usually have features with strong absorption as well as topographic phase effects near sharp jumps, such as edges and corners. The phase and intensity gradients tend to be non-collinear near corners, which generates a curl component in the in-plane Poynting vector as shown in the example mask in figure 3.3. Hence, in accordance with eqn. 3.9, the presence of Poynting vector curl causes the TIE solver in eqn. 2.5 to have residual phase errors.

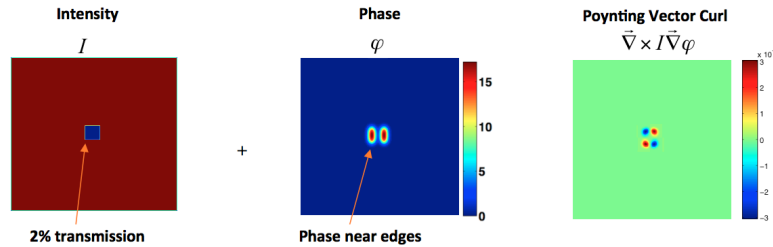


Figure 3.3: Strongly absorbing isolated contact feature on a clear mask with phase along the vertical edges shows non-zero curl in the Poynting vector near the corners of the feature, which gives rise to artifacts in the recovered phase. The simulation is designed to replicate experiments on an OMOG mask.

The errors in phase recovered by the TIE are shown in MATLAB simulations in figure 3.4. The feature simulated is an absorbing square block, 240nm in size, set in a clear field mask. The block has the same 2% transmission as an OMOG mask, and phase along the vertical edges replicating edge effects seen in real masks, as shown in fig. 3.4. The recovered phase has non-physical negative phase values along the horizontal edge, labeled in the recovered phase image as a saddle artifact. These artifacts severely degrade the accuracy of the result and need to be removed.

To correct artifacts due to the the curl, a second iteration of the solver is used to estimate the residual phase, in a manner similar to gradient descent. The recovered phase is plugged back into eqn. 2.1 to re-calculate the corresponding left hand side  $dI/dz$ . The estimated and original  $dI/dz$  values would be identical if the phase were recovered without artifacts. Hence their difference, the residual, is the error in the calculated phase, mostly due to the missing curl component in the solver. The residual can be input into the TIE solver to recover an

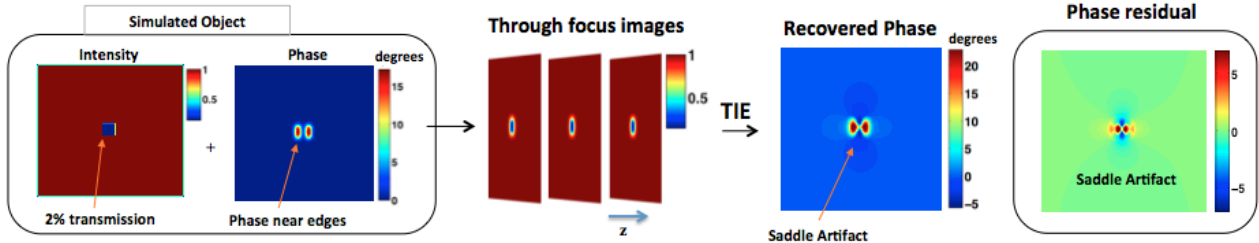


Figure 3.4: Simulations of a 98% absorbing object with phase near the absorption edges show that the phase recovered in areas of strong absorption tends to have non-physical artifacts when using the regular solver. The through-focus images are simulated in MATLAB and inverted as a Transport of Intensity equation from their  $\frac{dI}{dz}$  value at focus. The recovered phase has saddle artifacts due to curl effects, which can be corrected by the iterative solver.

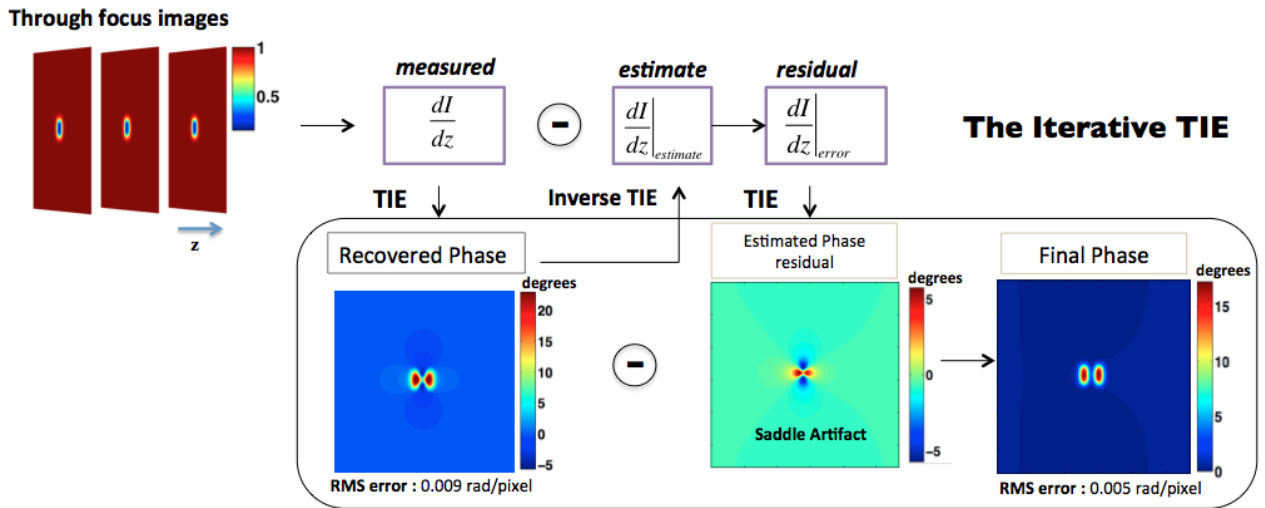


Figure 3.5: Schematic showing one iteration of the iterative TIE algorithm. Once the measured through-focus intensity gradient has been solved to recover the phase, the inverse solver is used to get an updated estimate of the gradient, which may not match measurements due to solver artifacts. The residual between the measured and estimated derivatives is solved again as a TIE equation to get the phase residual, which is subtracted from the recovered phase for an improved estimate.

estimate of the phase error, in this case the saddle artifact. The phase error estimate is then subtracted from the recovered phase to get an improved phase result, as shown in fig. 3.5. By implementing this simple recursion step we greatly improve the accuracy of the phase result. In the simulation shown, the RMS phase error dropped by about 42%, from 0.0087 radian/pixel to 0.005 radian/pixel after applying the modified algorithm.

The process can be extended to further iterations, similar to a conjugate gradient optimization [29]. The iterative method attempts to estimate some of the curl components which are missing in the divergence measurement of the TIE and lead to the spurious phase after the first run. Subsequent iterations measure parts of the solution that give residuals in another cycle of inverse and forward solving, which can be used to update the solution. Convergence of the solver depends on the object, the weights used in each iteration while subtracting the residual, and the severity of the curl error; a more rigorous formulation of the convergence remains to do be devised. The simulations shown here perform the first iterative step, which is seen to give the most benefit, further iterations yielding diminishing returns for this object.

## Chapter 4

# Measuring edge effects using quantitative phase imaging

In this chapter we measure edge effects experimentally by recovering the complex electromagnetic field at the wafer plane from intensity measurements, as also discussed in chapter 1, and shown in figure 1.3. An aerial-imaging tool [30] is used to measure a stack of through-focus images at the wafer plane of a projection printing system, from which the phase is calculated using the Transport of Intensity method described in chapters 2 and 3. We experimentally demonstrate the presence of edge effects using phase images, and quantify them for use in a thin mask simulator. Edge effects are found to be primarily in the direction of polarization (TM) as anticipated by Miller et al.[5], and shown in figure 4.1b. The experimental values presented in this work match well with the numbers from previously proposed boundary layer models, also shown in figure 4.1b.

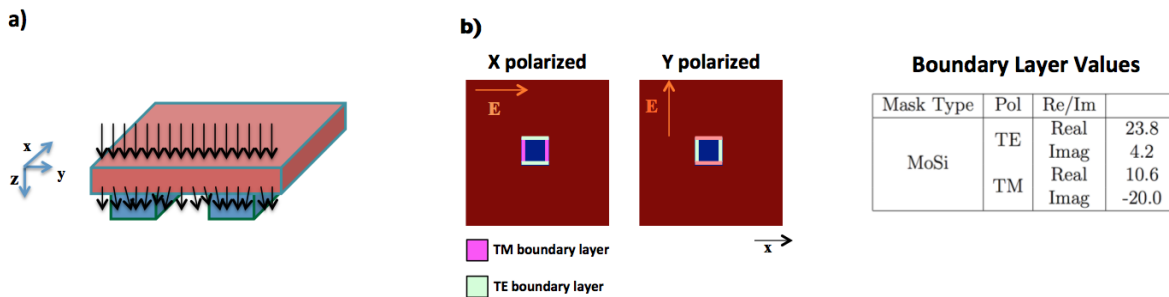


Figure 4.1: a) The 3D topography of attenuating masks causes diffraction near the feature edges, which shows up as phase edge effects at the wafer plane. b) Thick mask topographical effects can be modeled as polarization-dependent thin mask boundary layers. The boundary layers are complex valued, with real and imaginary parts for an ATT-PSM mask shown in the table.[5]

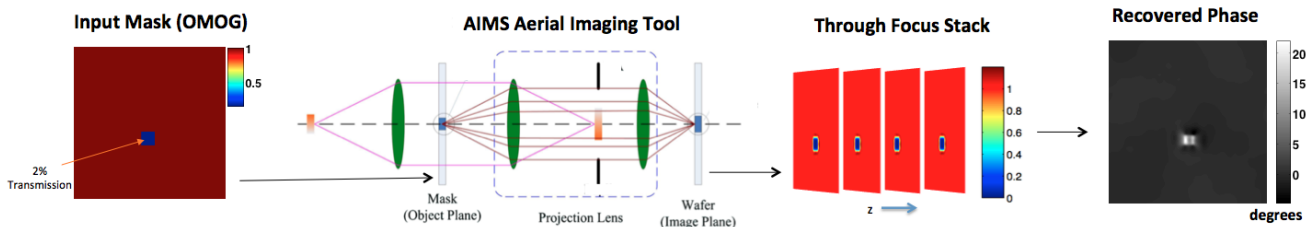


Figure 4.2: Aerial Imaging and Measurement System (AIMS) tool captures through-focus intensity images at the wafer plane from which the phase near the edges can be recovered. The mask is clear field OMOG with 2% absorber transmission, the absorbing feature is a 240nm isolated contact.

Sections 4.1 and 4.2 demonstrate the presence of edge effects using experimental phase images, and fit a thin mask boundary layer model to the observed phase, respectively. Section 4.3 compares the phase effects between OMOG and attenuating phase shift masks (ATT-PSM), showing that OMOG has about half the edge effects of phase shifting masks. Section 4.4 talks about the resolution and sensitivity of the phase imaging, and section 4.5 closes with a summary of the chapter.

## 4.1 Experiments on AIMS tool

The iterative TIE algorithm described previously is used to recover the wafer plane phase from intensity images measured on an Aerial Imaging and Measurement System (AIMS) at AMTC/Toppan Photomask Inc. located in Dresden, Germany.

A schematic of the tool is shown in Figure 4.2. The measurements are at a wavelength of 193nm, the illumination being on-axis monopole with a coherence sigma of 0.3. The NA of the imaging system is 1.4 and the field of view is 2.5um at the wafer. The defocus measurements were taken at 10nm steps up to a defocus depth of 50nm on both sides of focus at the wafer plane. The feature measured here is an absorbing isolated contact with a 240nm size and 2% transmission.

A comparison of the phase recovered with the regular TIE solver with that from the iterative solver is shown in figure 4.3. The iterative method seems to remove the artifacts from the regular solver after a single iteration. The recovered phase from the iterative TIE solver in Figure 4.4a shows the presence of edge effects in both directions, with the TM effects (in the direction of polarization) being dominant.

The edge effects are quantified as an angle-width product, since the product is a conserved quantity on passing through the imaging system, as described with simulations in the next section. The recovered images show that the absorber has an angle of about  $10^\circ$ , with phase bumps on top of the absorber angle due to diffraction at the thick mask edges. The edge effects are seen primarily in the direction of polarization, with an angle-width product of

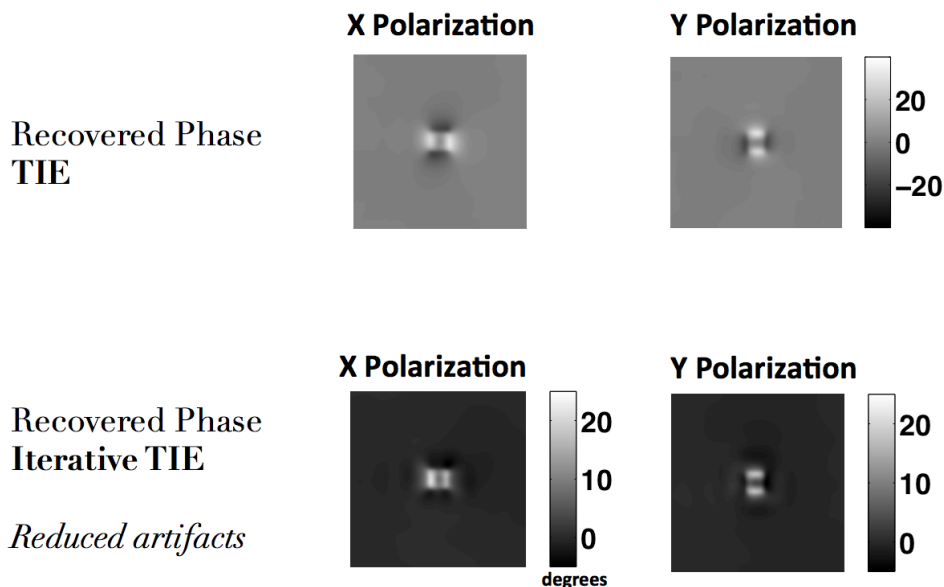


Figure 4.3: Phase recovered from experimental through-focus images for an OMOG mask shows errors with the TIE solver, which are mitigated with the help of an iterative method that estimates the error and subtracts it from the phase result in a subsequent iteration step.

$9^\circ \times 100nm = 900^\circ nm$  in the TM direction. The TE edge effects are about four times smaller, which is consistent with FDTD simulation values in the table of Fig. 4.1.

As expected, rotating the polarization rotates the TM direction (now in y direction), and hence the dominant edge effects are along the horizontal edges of the feature as shown in Figure 4.4b.

## 4.2 Comparison with thin mask boundary layer simulations

### Boundary layer spreading from mask to wafer

Thin mask boundary layer simulations approximate the edge effects seen in the experimental images at the wafer plane. The thin mask aerial image simulator (SPLAT[31]) replicates the projection printer coherence and numerical aperture from mask to wafer. Figure 4.5 shows simulations of a square feature with thin mask boundary layers.

The vertical edges of the square have boundary layers at  $90^\circ$  phase sitting on an absorber with  $10^\circ$  phase. The edge effects can be modeled as purely imaginary boundary layers ( $90^\circ$ ) as the real part amounts to a shift in the edge position, not affecting recovered phase. The sharp boundary layers are spread by the point spread function of the imaging system such

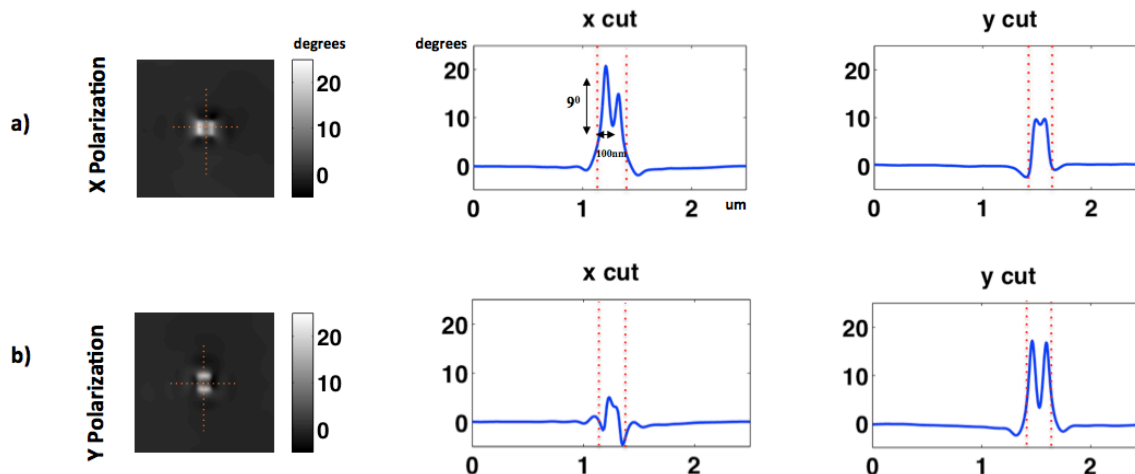


Figure 4.4: Phase recovery of edge effects in an OMOG mask a) Cutlines across the center of the feature show phase peaks at the location of edge effects. The edge effects are quantified as an angle $\times$ width product, which for the TM edge effect gives a value of  $900^\circ nm$ . b) Changing the direction of polarization changes the direction of the dominant edge effects. For x-polarized illumination, the dominant edge effects are along the x cutline in the TM direction. For y-polarized illumination, the dominant edge effects are still in the direction of polarization (TM), as seen in the y cutline.

that the angle  $\times$  width product is conserved at the wafer, as shown by the dotted red curve at the wafer plane. The angle-width product is hence used to quantify the edge effects in the phase images. Having measured the edge effects as phase bumps in the experimental images, simulating a mask with boundary layer width chosen according to the required angle-width product will allow for fitting the simulated wafer plane phase to experiment.

### Boundary layer fitting to experiment

A boundary layer of 10nm at a phase of  $90^\circ$  on the mask has the same angle-width product ( $900^\circ nm$ ) as the edge effects measured in the OMOG phase images in section 4.1. As the angle-width product is conserved from mask to wafer, the wafer plane images simulated in SPLAT replicate edge effects measured for OMOG mask at the wafer plane, as shown in Figure 4.6.

Here, vertical boundary layers are used to compare against the phase for an OMOG mask under x-polarized illumination. The corresponding fitting can also be done for y-polarized light, in which case the boundary layers would be added to the horizontal edges of the block. The method is an effective deconvolution but with a priori information about the mask

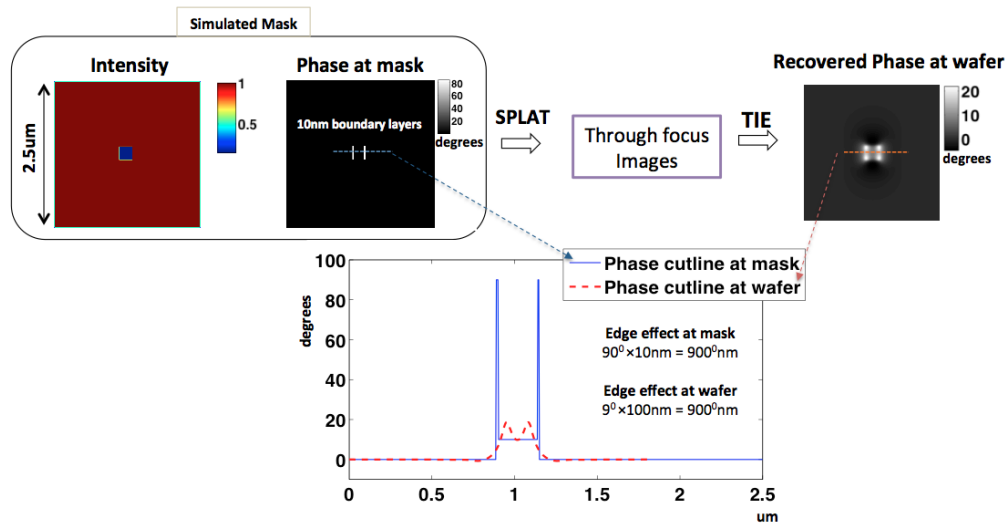


Figure 4.5: SPLAT thin mask simulations show that the spreading of the mask boundary layer at wafer by the imaging system conserves the angle-width product. The blue and red cutlines correspond to the phase at mask and wafer. Both cutlines show an absorber angle of  $10^\circ$  near the center of the block, with the red cutline having spread on going through the imaging system, such that the peak angle measured from the substrate is inversely reduced to preserve the height-width product.

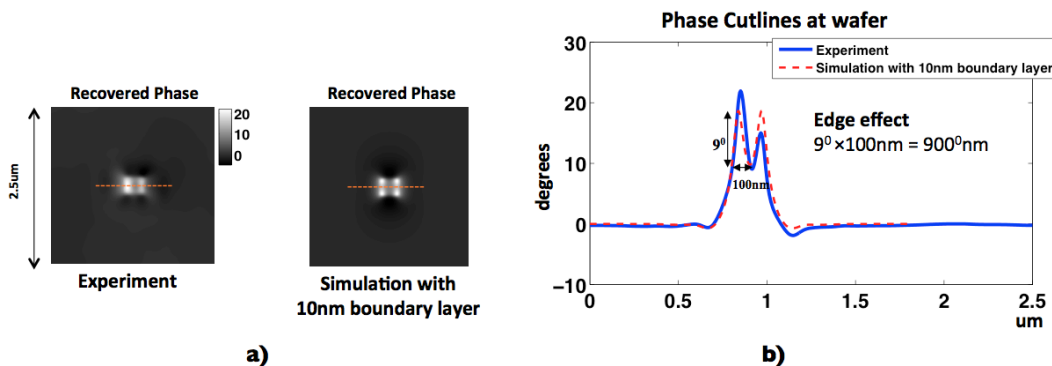


Figure 4.6: Thin mask simulations with quadrature phase ( $90^\circ$ ) boundary layers fit the phase recovered from experiments with OMOG mask. a) Simulation performed with vertical boundary layers are compared with experiments with x-polarized light. The mask boundary layer is at an angle of  $90^\circ$ , with the width chosen to be  $10\text{nm}$  ( $900^\circ\text{nm}$ ). b) Cutlines comparing wafer plane phase for simulation and experiment. The angle-width product stays conserved for the red line (simulation) from mask to wafer, which agrees with the blue line from experiment, with a corresponding angle-width product of  $900^\circ\text{nm}$ .

feature, it being assumed that the boundary layers on the mask are at a  $90^\circ$  phase angle. An extension of this approach would allow direct modeling of thin mask effective boundary layers from measured phase at wafer plane for any general feature type.

### 4.3 Measured edge effects in OMOG vs. ATT-PSM

One of reasons cited for the migration to OMOG masks for printing smaller node sizes is the smaller values of the expected edge effects at the wafer, resulting in improved through-focus behavior and requiring lesser OPC correction [1]. Here we compare the edge effects for x-polarized illumination in an OMOG mask with an attenuating phase shift mask (ATT-PSM), as shown in Figure 4.7.

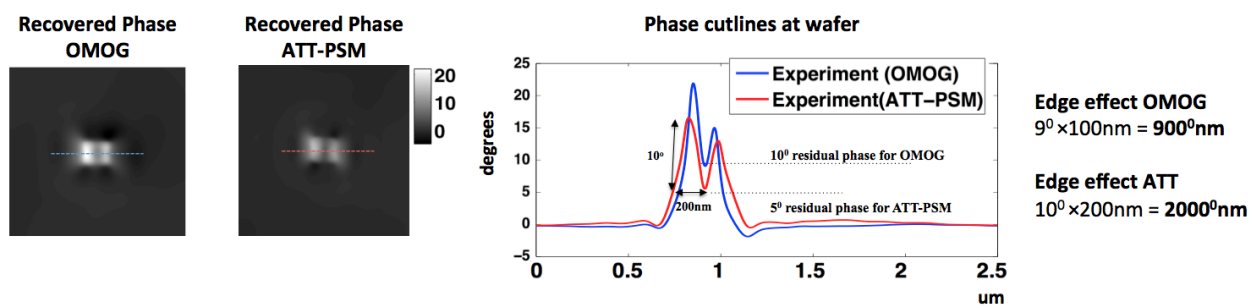


Figure 4.7: Comparing edge effects in phase shift mask (ATT-PSM) and OMOG for x-polarized light. a) The edge effects are in the direction of the polarization in both cases. b) Overlapping the phase cutlines shows that the ATT-PSM has an absorber angle of  $5^\circ$ , corresponding to a real angle of  $185^\circ$ , compared to  $10^\circ$  for OMOG. The edge effects are about the same height, but the ATT-PSM has twice the spread when compared with OMOG.

The phase cutlines show that the angle-width product for the phase bumps due to edge effects is about twice as much in the ATT-PSM than OMOG mask, as expected, due to larger topographical variations on the phase shift mask vs OMOG.

### 4.4 Limitations

The phase images have the same resolution limitations as the intensity images, given by the Rayleigh criterion, in this case  $\frac{\lambda}{NA} \approx 137nm$  is the size of the point-spread function. Hence edge effects for features smaller than the resolution limit cannot be resolved directly, as shown in Figure 4.8. The phase bumps due to edge effects in the 240nm feature are well resolved, but merge into a single peak for a 120nm feature, where the peaks are closer than the point spread function of the imaging system.

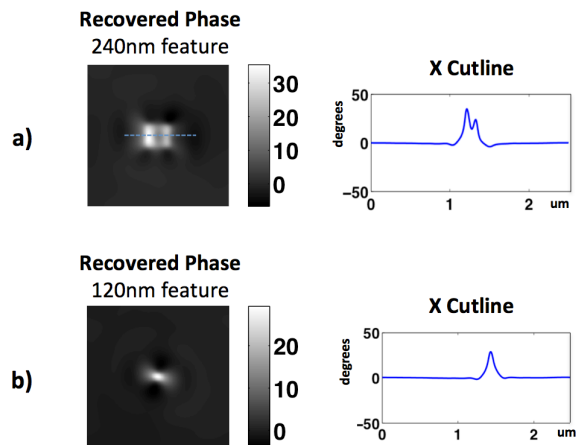


Figure 4.8: Edge effects for two features sizes above and below the resolution limit of the imaging system, for x-polarized illumination. a) A 240nm square has two distinct peaks in the x-cutline, the edge effects for the two vertical edges are resolved in the phase image. b) Shrinking the feature size to below the resolution limit to 120nm makes the peaks indiscernible, a single peak seen in the x-cutline of the recovered phase image.

Indirect methods could still be used to achieve effective super-resolution, i.e. resolution beyond the diffraction limit, similar to super-resolution techniques in fluorescence microscopy. Given the knowledge that the unresolved function is the sum of two identical edge spread functions, the individual functions can in principle be identified from their unresolved sum.

Besides lateral resolution, the other key metric for TIE performance is phase sensitivity. The TIE (eqn. 2.1) solves for phase from changes in the intensity through focus; hence the smallest phase that can be imaged by the system depends on the sensitivity of the camera to small changes in intensity, i.e. its dynamic range. In these experiments, however, the noise in the intensity measurement is much larger than the dynamic range of the camera, and hence the phase sensitivity is limited to the noise in the phase estimate. Figure 4.9 shows a simulation of noise in the recovered phase due to noise in the intensity. At intensity noise comparable with experimental data, the phase has rms noise of about one-hundredth of a degree per pixel. This is a rough estimate of the phase sensitivity of the method, and is two orders of magnitude smaller than the signal due to edge effects seen in the measurements.

## 4.5 Conclusions

Thick mask topography causes phase effects near edges, which behave like imaginary ( $90^\circ$  phase) boundary layers being imaged to the wafer plane. We have experimentally observed the presence of these edge effects by looking at phase images extracted from intensity images

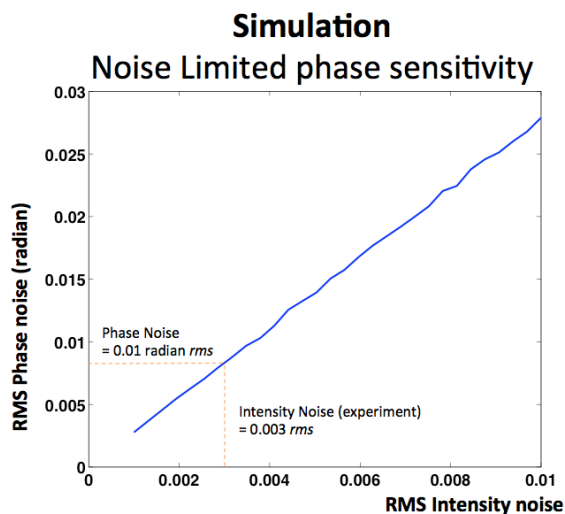


Figure 4.9: The phase sensitivity is limited by the noise in the intensity measurements. A simulation of rms noise in the recovered phase with increasing noise in the intensity shows a linear dependence. The experiments have rms noise of about 0.003; the corresponding phase noise is 0.01radian/pixel, two orders of magnitude smaller than the phase signal due to edge effects.

on an aerial imaging tool (AIMS). The phase imaging algorithm is a modification of the Transport of Intensity equation (TIE) to correct for strong absorption artifacts in the TIE solver. A stack of through-focus images is used to recover the in-focus phase, which shows edge effects predominantly in the direction of polarization, as anticipated by previous work using full wave simulations. These edge effects are quantified by their peak-angle times width product, which is shown to be conserved in thin mask simulations from mask to wafer. A thin mask boundary layer model is then shown to fit the edge effects in OMOG, an approach which might be extended to boundary layer estimation for more general features. Next the boundary layer values for ATT-PSM and OMOG are compared, showing that OMOG has about half the edge effects as ATT-PSM. The results agree with the edge effects predicted by full wave simulations cited in fig. 4.1, which predict 20nm boundary layers at the mask for ATT-PSM and hence half the value for OMOG at 10nm, also found to be the case here. The sensitivity of the phase imaging is noise limited, the limit being a couple of orders of magnitude smaller than the phase near the edges seen in experiments. At the same time the phase-image resolution depends on the wavelength and numerical aperture, with the possibility of effective super-resolution once the phase spread function of feature edges has been characterized.

## Chapter 5

# The TIE with non-uniform illumination

The Transport of Intensity equation (TIE) solves for the complex field at the plane of interest by using intensity measurements from a detector moved through multiple defocus planes. Patterning the illumination allows the possibility of multiplexing at the source instead of the detector, allowing fast recovery of quantitative phase without the need for moving the sample or camera.

For plane wave illumination, the complex field is the object itself; for patterned illumination, the field is a product of the object and illumination. In this chapter an extended framework for the TIE is presented which models the defocus behavior of light for arbitrary illumination patterns, thus providing a common framework for describing structured illumination[32], shearing interferometry[33, 34], and defocus based imaging methods[14, 35]. It is further shown that the illumination modulation provides an extra degree of freedom which can be used to devise alternative schemes for phase recovery from intensity measurements.

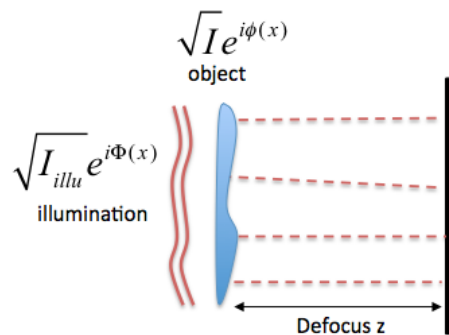


Figure 5.1: Schematic illustrating a patterned illumination, represented as complex field  $\sqrt{I_{illu}} e^{i\Phi}$ , interacting with a thin sample,  $\sqrt{I} e^{i\phi}$ , and propagating to defocus.

Figure 5.1 shows an illumination,  $\sqrt{I_{illu}}e^{i\Phi}$ , incident on a sample,  $\sqrt{I}e^{i\phi}$ . The intensity at focus is the product of the object and illumination intensities,  $I_{total} = I_{illu}I$ , and the phase is the sum of the respective phases,  $\phi_{total} = \phi + \Phi$ . Substituting directly into the TIE of eqn 2.1,

$$-k\frac{\partial I}{\partial z} = \vec{\nabla} \cdot I_{total} \vec{\nabla} \phi_{total} = \vec{\nabla} \cdot I_{illu} I \vec{\nabla} \{\phi + \Phi\} \quad (5.1)$$

Equation 5.1 can be expanded by the product rule of derivatives; the expansion is simplified for the the special cases of constant illumination intensity and constant illumination phase, as described below in sections 5.1 and 5.2 respectively.

## 5.1 Patterning illumination phase

If the illumination is a pure phase modulation, it has constant intensity and can be written as  $1e^{i\Phi(x,y)}$ , thus removing terms with  $\nabla I_{illu}$  dependence from the product expansion of equation 5.1,

$$\begin{aligned} \vec{\nabla} \cdot I \vec{\nabla} \{\phi + \Phi\} &= -k \frac{\partial I}{\partial z} \\ \Rightarrow \vec{\nabla} \cdot I \vec{\nabla} \phi + \vec{\nabla} \cdot I \vec{\nabla} \Phi &= -k \frac{\partial I}{\partial z} \end{aligned} \quad (5.2)$$

where  $I$  and  $\phi$  are the object intensity and phase respectively, while  $\Phi$  is the illumination phase. The first term on the LHS is the familiar defocus term for plane wave illumination, and the second term describes the effect of the illumination phase on the defocus intensity. An example of an illumination with pure phase modulation is a tilted plane wave, for which the illumination phase is a linear ramp  $\Phi = \alpha_1 x + \alpha_2 y$ , reducing phase gradient  $\vec{\nabla} \Phi$  in equation 5.2 to a constant,

$$\vec{\nabla} \cdot I \vec{\nabla} \phi + \hat{\alpha} \cdot \vec{\nabla} I = -k \frac{\partial I}{\partial z} \quad (5.3)$$

where  $\hat{\alpha} = \alpha_1 \hat{x} + \alpha_2 \hat{y}$  is the two dimensional k-space illumination vector (zero for on-axis illumination). The extra term,  $\hat{\alpha} \cdot \vec{\nabla} I$ , can be understood as a lateral shift in the at-focus intensity  $I$ , seen the corresponding Taylor series expansion,

$$\begin{aligned} I(x + \alpha z) &= I(x) + \alpha z \nabla I(x) + \frac{\alpha^2 z^2}{2} \nabla^2 I + \dots \\ \Rightarrow \alpha \nabla I &\approx \frac{I(x + \alpha z) - I(x)}{z} \end{aligned}$$

where a paraxial approximation allows us to drop higher order terms in  $\alpha z$ . Hence a tilted plane wave illumination shifts the object's at-focus intensity laterally in proportion to the angle of illumination and the defocus distance. Illumination from extended sources can be modeled as a summation of incoherent plane waves, each point on the source contributing a  $\hat{\alpha}$  term to equation 5.3, as described earlier in section 2.5.

## 5.2 Patterning illumination intensity

For illumination with only intensity modulation and constant phase, the product expansion in equation 5.1 loses terms with  $\Phi$  dependence. Setting the illumination to be  $I_{illu}$  in equation 5.1,

$$\begin{aligned} \vec{\nabla} \cdot I_{illu} I \vec{\nabla} \phi &= -k \frac{\partial I}{\partial z} \\ \Rightarrow I_{illu} \vec{\nabla} \cdot I \vec{\nabla} \phi + I \vec{\nabla} I_{illu} \cdot \vec{\nabla} \phi &= -k \frac{\partial I}{\partial z} \end{aligned} \quad (5.4)$$

The first term is the illumination weighted defocus term of the object; the second term is the shift in the illumination pattern on defocusing due to phase gradients in the object. The Transport of Intensity equation (eqn 2.1) solves for the defocus term, which depends on the object phase as a second derivative. The second term, on the other hand, has a first derivative dependence on phase. Solving the phase from its first derivative can be expected to provide better signal to noise performance at low frequencies, as observed when comparing the transfer functions of the first and second derivatives across spatial frequencies, shown in figure 5.2. The Transport of Intensity solvers that invert the second derivative typically suffer from low frequency noise in the reconstructed phase due to the vanishing signal at zero frequencies, and hence improving signal at low frequencies is a significant benefit. The signal at higher frequencies is robust for both the first and second derivatives, and hence high frequencies are fairly resilient to noise in either case.

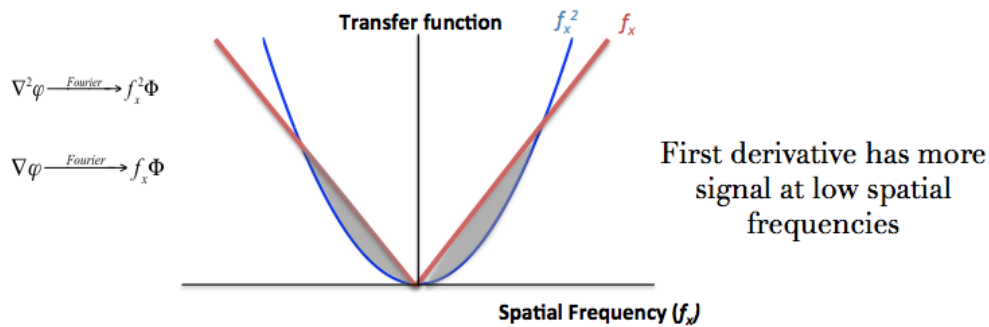


Figure 5.2: Comparison of the transfer functions of the first and second derivative shows that the first derivative provides more signal at lower frequencies, and is hence more robust to low frequency noise in the reconstructed phase.

## Calculating the phase gradient

As motivated in the previous section, an illumination scheme that can isolate the first gradient of phase might be preferable over second-derivative defocus based methods in the presence of measurement noise. The intensity  $I$  of the illumination can be modulated to isolate the phase gradient from equation 5.4. To demonstrate this, we write the RHS as a finite difference,

$$I_{illu} \vec{\nabla} \cdot I \vec{\nabla} \phi + I \vec{\nabla} I_{illu} \cdot \vec{\nabla} \phi = -k \frac{I_{z,illu} - I_{illu} I}{\Delta z}$$

where the product of object and illumination intensities,  $I_{illu} I$ , is the at-focus intensity, and  $I_{z,illu}$  is the corresponding defocus intensity. The equation has two terms on the left hand side, the defocus term (second derivative in phase) and the illumination gradient term (first derivative in phase). If the illumination is then switched to a plane wave with  $I = 1$ , the equation reduces to the usual TIE equation,

$$\vec{\nabla} \cdot I \vec{\nabla} \phi = -k \frac{I_z - I_{illu}}{\Delta z}$$

with only the object defocus term due to absence of structure in the illumination. Scaling the second equation by illumination  $I_{illu}$  and combining with the first isolates the phase gradient term,

$$I \vec{\nabla} I_{illu} \cdot \vec{\nabla} \phi = -k \frac{I_{z,illu} - I_{illu} I_z}{\Delta z} \quad (5.5)$$

$I_{z,illu}$  and  $I_z$  are intensity values at the defocus plane. Hence measurements with a structured illumination pattern and a plane wave illumination pattern at a single defocus plane can be used to calculate the phase gradient of the sample,  $\vec{\nabla} \phi$ , given the illumination intensity  $I_{illu}$  and the object intensity  $I$  are known, as described in the following set of examples.

## 5.3 Recovering phase using patterned illumination

Recovering the phase using illumination patterning offers the advantage of not requiring moving parts in the system, as multiple measurement can be taken for different illumination settings at the same defocus plane. The method recovers the first gradient information at the position of illumination gradients,  $\vec{\nabla} I_{illu}$ , as seen in equation 5.5, and hence can be used to solve for phase gradients with any illumination which has structure in its intensity. The examples that follow use sinusoid intensity patterns as they uniformly sample the phase gradients in the sample, and are easily produced on a deformable mirror device.

### Simulations with a phase phantom

The phase gradient from equation 5.5 can be recovered with the help of two intensity measurements,  $I_{z,illu}$  and  $I_z$ , measured at the same defocus plane with and without illumination

### Step I. Intensity Measurements

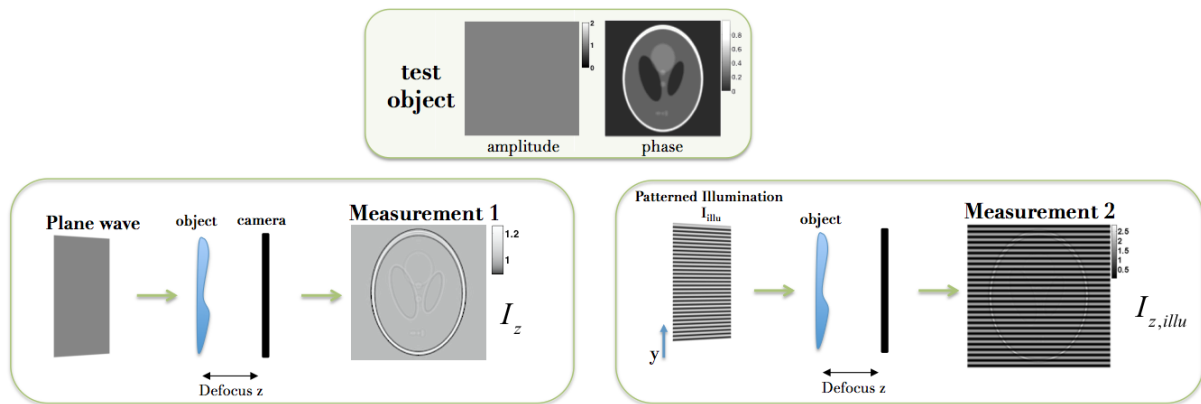


Figure 5.3: Defocus measurements with patterned illumination can be used to recover the phase gradient of a simulated phase object. The figure shows intensity images of a phantom phase object that is numerically propagated to defocus distance  $z$  with a plane wave illumination and sinusoid illumination pattern respectively.

### Step II. Extracting the refraction term

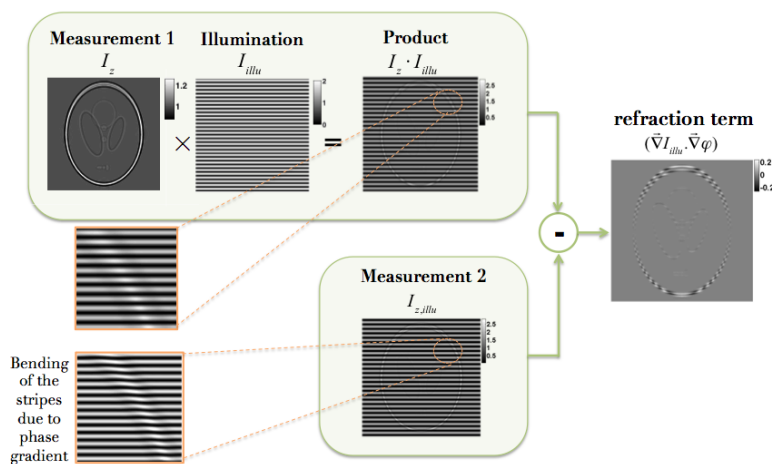


Figure 5.4: The two defocus intensity measurements with the patterned illumination and the plane wave illumination can be combined to extract the refraction term, i.e. the product of the phase gradient and illumination gradient, which is demodulated in a further step.

Step III. Demodulating the refraction term

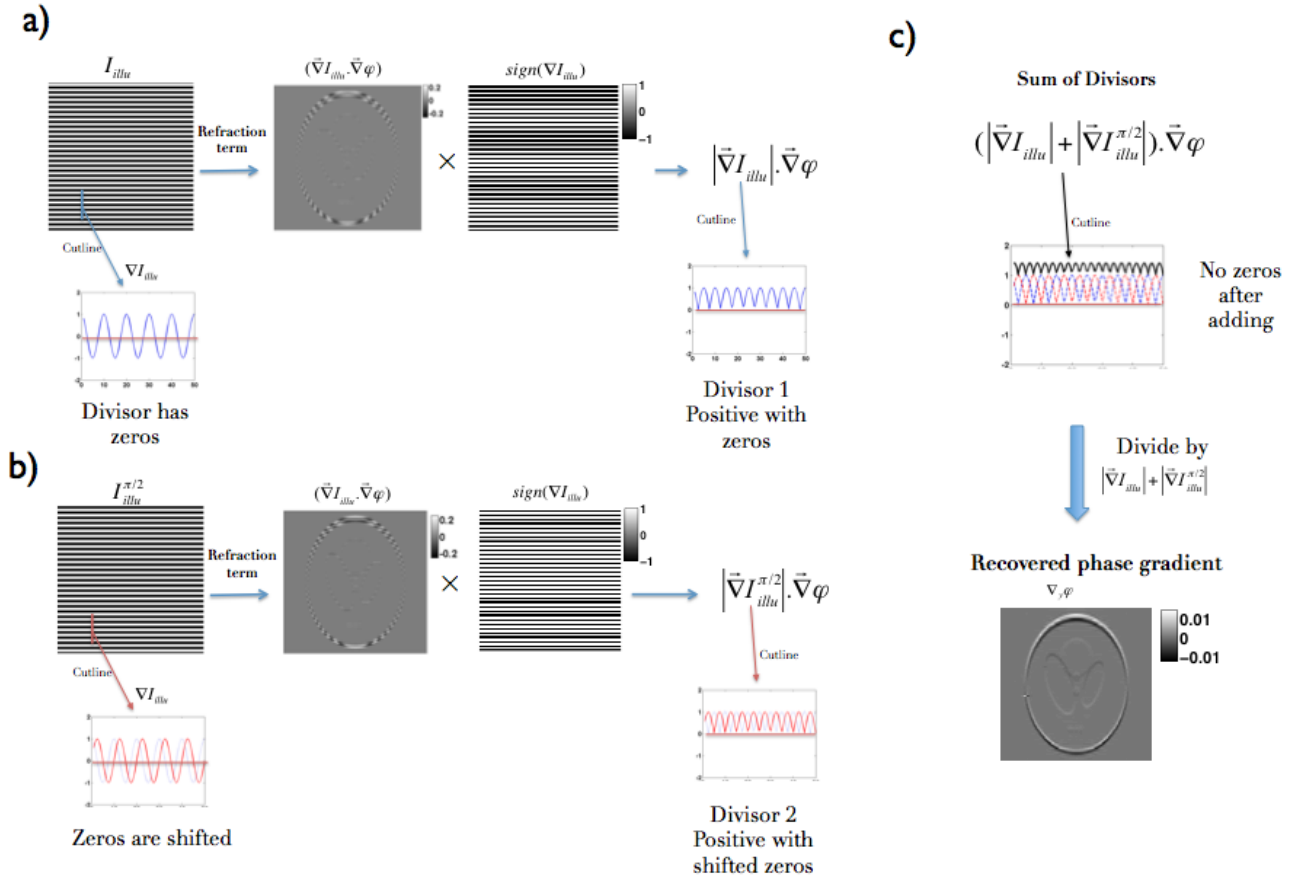


Figure 5.5: Schematic showing the demodulation of the refraction term, the product  $\nabla I \cdot \nabla \phi$ , using two stripe patterns shifted by a quarter period. a) The product  $\nabla I \cdot \nabla \phi$  is multiplied by the sign of the illumination gradient, which makes the divisor of the phase gradient purely positive, albeit still with zeros. b) Performing the same procedure for the pattern shifted by quarter of the period shifts the position of the zeros. c) Addition of the resulting patterns has no zeros in the divisor, which can be directly divided to recover the phase gradient in the direction normal to the stripes,  $\nabla_y \phi$ .

patterning. A simulation object is chosen with a phantom phase and uniform intensity as shown in figure 5.3. The defocus intensities on illuminating with a plane wave and a sinusoidal stripe pattern are shown at a fixed defocus distance. The phase gradient of the object couples to the intensity gradient of the stripe patterns, hence the phase gradient is sampled at the rate of the sinusoid period. Horizontal stripes are used to recover y-gradient of the object phase, and likewise vertical ones for the x-gradient.

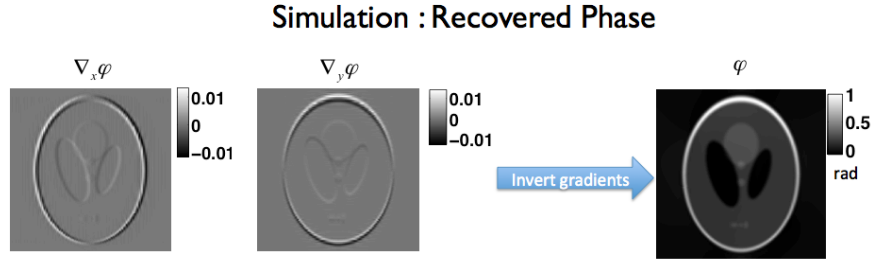


Figure 5.6: The phase gradients extracted from structured illumination in either direction can be combined to reconstruct the two dimensional phase, in this case a phantom phase object.

Figure 5.4 shows the operation equivalent to the right hand side of equation 5.5, where the defocus intensities with the patterned illumination and a plane wave illumination are combined to extract the refraction term  $\vec{\nabla} I_{illu} \cdot \vec{\nabla} \phi$ . The plane wave defocus measurement is scaled by the stripe pattern, and subtracted from the defocus measurement with the striped illumination incident on the sample to calculate the stripe bending due to the phase gradient  $\nabla_y \phi$ .

Figure 5.5 shows the demodulation procedure, which performs full resolution reconstruction by combining the calculated refraction term from two shifted illumination patterns. The need for the a second shifted sinusoid illumination can be thought of as a sampling requirement for full resolution reconstruction. A single sinusoid will sample only at positions of non-zero intensity gradient, implicit in the measurement  $\vec{\nabla} I_{illu} \cdot \vec{\nabla} \phi$ , and hence a shifted pattern effectively fills in the zeros of the first to return the phase gradient information at full resolution.

The demodulation algorithm is shown in fig. 5.5. An extra step of multiplying by the sign of the illumination gradient makes the measured refraction term the product of a positive quantity,  $|\nabla I_{illu}|$ , with the phase gradient ( $\nabla \phi$ ). Adding the result from the two shifted illuminations makes the premultiplier,  $|\nabla I_{illu}| + |\nabla I_{illu}^{\pi/2}|$ , free of zeros, and it can subsequently be divided out to recover the phase gradient  $\nabla_y \phi$ .

The phase gradient in the x direction can be likewise calculated using the corresponding stripe pattern rotated by  $90^\circ$ , followed by the quarter period shifting method for demodulation. Gradients in two directions are then combined and solved for phase, as shown Figure 5.6. The phase inversion from the gradient measurements is performed by adding the divergence of the gradients to convert them to scalar fields, as follows,

$$\vec{\nabla} \cdot \vec{\nabla}_x \phi(x, y) + \vec{\nabla} \cdot \vec{\nabla}_y \phi(x, y) = \nabla^2 \phi(x, y) \quad (5.6)$$

which can be solved using a Poisson solver to recover the phase  $\phi$ . The Poisson solver is the same as that used for the TIE, in which case, however, the second gradient is directly

recovered from measurements and put into the Poisson solver.

Using more shifted measurements makes the multiplier better behaved, and should return a better result in the experimental case in the presence of noise. Additionally, gradients in directions intermediate between  $x$  and  $y$  can be used to fill the gradient circle and help the robustness of the gradient inversion technique against noise.

## Experiment

An experimental setup for structured illumination phase recovery is shown in figure 5.7. A binary deformable mirror device is used to structure the illumination of the incident light. Using a deformable mirror device allows rapid illumination patterning at the rate of 20kHz, and enables the precise quarter pitch shifting of the structured pattern needed for full resolution phase recovery by the proposed method. A 40x objective images the mirror onto the microscopic cheek cell sample, with a mirror image of the de-magnifying setup re-imaging the resulting field onto the camera. The camera is placed at a defocus plane of the sample, the ideal defocus distance depending on the phase gradients in the sample, pitch of the sinusoid illumination, and the partial coherence of the incident beam. Higher defocus distances give a stronger refraction term for a given object, but would have reduced contrast in the presence of partial coherence, introduced here using a rotating diffuser before the DMD.

The phase recovered by applying the the demodulation process described earlier is shown in figure 5.8. The gradient images recovered are at the full resolution of the imaging system, as no low pass filtering has been applied in the gradient extraction. The phase can be inverted using gradients in two direction as described earlier for simulations. The method presented here is generally applicable for any patterned illumination, with the resolution and contrast of the recovered phase limited only by the gradients in the intensity pattern of the incident illumination.

## Conclusions

We have demonstrated a scheme for extracting the phase of a transmitting sample in an imaging system simply by patterning the illumination incident on the sample, and taking measurements at a fixed defocus plane. The phase gradient of the object couples to gradients in the illumination structure on defocusing, which can be inverted to solve for phase gradient and subsequently for phase. The method requires no moving parts in the imaging system between measurements, and hence is self aligning and free from registration issues commonly encountered in techniques that use information from multiple defocus planes. It might be especially applicable to systems such as X-Ray beamlines and EUV tools, where wavelengths are small enough to require large defocus steps for TIE-like methods, making measurements at multiple planes cumbersome. By illumination modulation instead, the defocusing is replaced with the insertion of a patterning mask before the object, simplifying the measurement scheme in the presence of the requisite patterning capability.

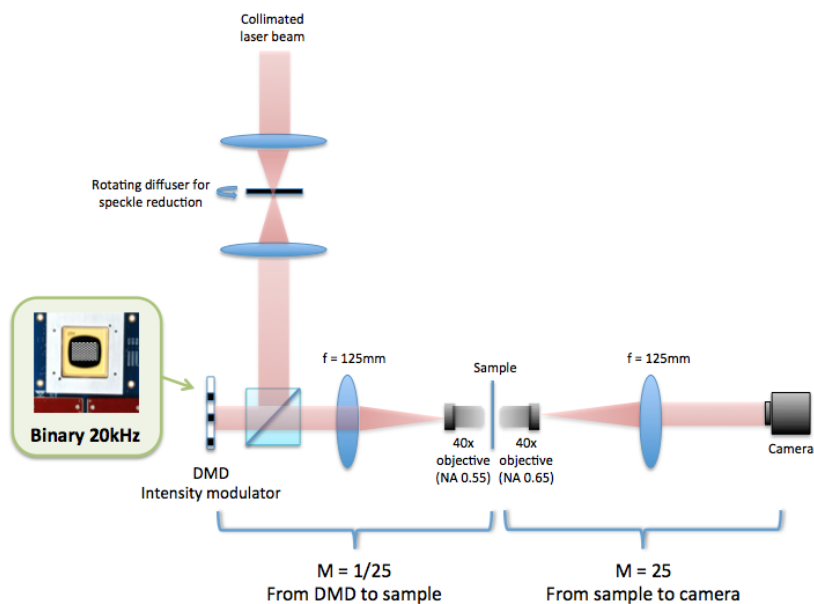


Figure 5.7: Schematic showing the experimental setup for the recovery of the first order phase gradient using structured illumination. A binary deformable mirror device is used to structure the illumination, which is demagnified and focused onto the cheek cell sample using a  $40\times$  objective. The resultant field is magnified with another objective and imaged onto the camera, which is at an effective defocus plane of the sample.

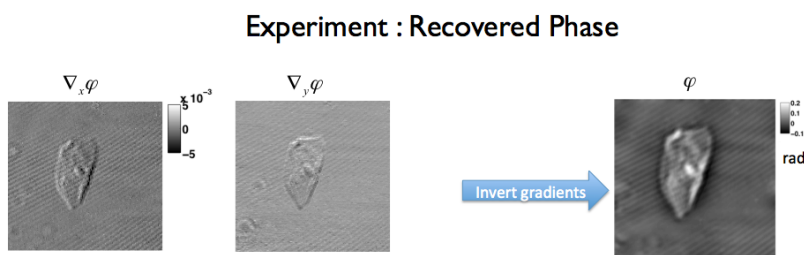


Figure 5.8: The phase gradients extracted from structured illumination in orthogonal directions  $x$  and  $y$  can be combined to reconstruct the two dimensional phase for a cheek cell.

# Chapter 6

## Summary and Future work

It has been shown that phase images recovered from the Transport of Intensity model of through-focus light propagation can identify topography induced edge effects in photomasks. The algorithm used has not been specifically modified for the partially coherent case with an extended source, but is shown to be resilient to partial coherence, and hence the phase images are still reliable for a source with  $\sigma = 0.3$ . The method can be expected to break, however, as one increases the size of the source, a common trick used by lithographers to increase resolution by pushing more frequencies through the numerical aperture of the system. An extension of the method that can include the shape of the source and the numerical aperture of the system would have to add intensity images from each coherent mode of the illumination, at the same time accounting for the bandwidth of the imaging system. Each mode corresponds to a single point on an extended Koehler source, shifting the spectrum of the object by a different amount in the bandlimited pupil. This will have to be included in the deconvolution algorithm that accounts for blurring in through-focus images due to source shape.

It was also shown that the height-width product of the phase bumps at feature edges is conserved from mask to wafer, an assumption that relies on the phase edges being resolved while measuring the width at the base of the bumps. For phase bumps closer than the resolution limit of the imaging system, indirect methods might have to be used for their quantification. Additionally, the observed linear behavior of the phase spread as the field passes through the imaging system can be expected to change in the presence of modified coherence. Hence a detailed study, with various source shapes and sizes, would be needed to characterize the validity of the boundary layer model and the expected linearity of modeled boundary layers on propagation through the imaging system.

Other system parameters that influence the accuracy of the final phase result need be characterized for performance analysis. The phase imaging methods are object, illumination, noise and defocus step dependent. Taking more images at each step helps with noise, and taking more images in the through focus stack gives a better estimate of the z derivative of intensity and hence also of the recovered phase. The optimum number and position of measurements is also object and algorithm dependent, and can be optimized for a given tool

and mask.

The iterative method described is generally applicable to any object with a curl in the in-plane power flow. In the presence of curl, running the solved phase backward through the solver leaves a residual in the through-focus intensity derivative. The residual is solved for in an iterative step and subtracted from the phase result, and so on for subsequent iterations. The convergence of the method depends on the weight applied to the residual phase at each step when correcting the phase result from the previous step. A rigorous formulation of the convergence criteria might be object and solver dependent, and hence a heuristic criteria might have to suffice. The optimal number of iterative steps is also a trade-off between computation time and desired accuracy of the result, the maximum improvement for the test cases seen to be in the first couple of iterations of the algorithm. Hence a general framework for the iterative algorithm will be able to provide bounds on the convergence for any given feature type.

# Bibliography

- [1] Tom Faure et al. In: *Photomask Technology 2010*. Ed. by M. Warren Montgomery and Wilhelm Maurer. SPIE-Intl Soc Optical Eng, 2010, 78230J–78230J–12. URL: <http://dx.doi.org/10.1117/12.864130>.
- [2] K. Adam and A.R. Neureuther. “Simplified models for edge transitions in rigorous mask modelling”. In: *Proc. of the SPIE* 4346 (2001), pp. 331–344.
- [3] J. Tirapu-Azpiroz, P. Burchard, and E. Yablonovitch. “Boundary layer model to account for thick mask effects in photolithography”. In: *Society of Photo-Optical Instrumentation Engineers (SPIE) Conference Series*. Ed. by A. Yen. Vol. 5040. Society of Photo-Optical Instrumentation Engineers (SPIE) Conference Series. June 2003, pp. 1611–1619. DOI: 10.1117/12.488803.
- [4] Jaione Tirapu Azpiroz et al. “Critical impact of mask electromagnetic effects on optical proximity corrections performance for 45 nm and beyond”. In: *Journal of Vacuum Science Technology B: Microelectronics and Nanometer Structures* 25.1 (2007), pp. 164–168. DOI: 10.1116/1.2429667. URL: <http://link.aip.org/link/?JVb/25/164/1>.
- [5] Marshal Miller. “Mask Edge Effects in Optical Lithography and Chip Level Modeling Methods”. PhD thesis. EECS Department, University of California, Berkeley, 2010. URL: <http://www.eecs.berkeley.edu/Pubs/TechRpts/2010/EECS-2010-160.html>.
- [6] J. R. Fienup. “Phase retrieval algorithms: a comparison”. In: *Appl. Opt.* 21.15 (1982), pp. 2758–2769. URL: <http://ao.osa.org/abstract.cfm?URI=ao-21-15-2758>.
- [7] J. Fienup. “Iterative method applied to image reconstruction and to computer-generated holograms”. In: *Optical Engineering* 19.3 (1980), pp. 291–305.
- [8] R. Gerchberg and W. Saxton. “A practical algorithm for the determination of phase from image and diffraction plane pictures”. In: *Optik* 35 (1972), pp. 237–246.
- [9] Michael Reed Teague. “Deterministic phase retrieval: a Green’s function solution”. In: *J. Opt. Soc. Am.* 73.11 (1983), pp. 1434–1441. DOI: 10.1364/JOSA.73.001434. URL: <http://www.opticsinfobase.org/abstract.cfm?URI=josa-73-11-1434>.
- [10] N. Streibl. “Phase imaging by the transport equation of intensity”. In: *Optics Communications* 49 (Feb. 1984), pp. 6–10. DOI: 10.1016/0030-4018(84)90079-8.

- [11] J. H. Poynting. “On the Transfer of Energy in the Electromagnetic Field”. In: *Philosophical Transactions of the Royal Society of London* 175 (1884), pp. 343–361. DOI: 10.1098/rstl.1884.0016. eprint: <http://rstl.royalsocietypublishing.org/content/175/343.full.pdf+html>. URL: <http://rstl.royalsocietypublishing.org/content/175/343.short>.
- [12] V.V Volkov and Y Zhu. “Lorentz phase microscopy of magnetic materials”. In: *Ultramicroscopy* 98.2â“4 (2004). Festschrift in Honor of the 70th Birthday of Professor Fang-Hua Li, pp. 271 –281. ISSN: 0304-3991. DOI: <http://dx.doi.org/10.1016/j.ultramicro.2003.08.026>. URL: <http://www.sciencedirect.com/science/article/pii/S0304399103002079>.
- [13] Zhong Jingshan et al. “Efficient Gaussian Inference Algorithms for Phase Imaging”. In: *Proc. IEEE ICASSP* (2012), pp. 25–30.
- [14] L.J. Allen and M.P. Oxley. “Phase retrieval from series of images obtained by defocus variation”. In: *Optics Communications* 199.1–4 (2001), pp. 65 –75. ISSN: 0030-4018. DOI: [http://dx.doi.org/10.1016/S0030-4018\(01\)01556-5](http://dx.doi.org/10.1016/S0030-4018(01)01556-5). URL: <http://www.sciencedirect.com/science/article/pii/S0030401801015565>.
- [15] T.E Gureyev and K.A Nugent. “Rapid quantitative phase imaging using the transport of intensity equation”. In: *Optics Communications* 133.1–6 (1997), pp. 339 –346. ISSN: 0030-4018. DOI: [http://dx.doi.org/10.1016/S0030-4018\(96\)00454-3](http://dx.doi.org/10.1016/S0030-4018(96)00454-3). URL: <http://www.sciencedirect.com/science/article/pii/S0030401896004543>.
- [16] V.V. Volkov, Y. Zhu, and M. De Graef. “A new symmetrized solution for phase retrieval using the transport of intensity equation”. In: *Micron* 33.5 (2002), pp. 411 –416. ISSN: 0968-4328. DOI: [http://dx.doi.org/10.1016/S0968-4328\(02\)00017-3](http://dx.doi.org/10.1016/S0968-4328(02)00017-3). URL: <http://www.sciencedirect.com/science/article/pii/S0968432802000173>.
- [17] Laura Waller, Lei Tian, and George Barbastathis. “Transport of Intensity phase-amplitude imaging with higher order intensity derivatives”. In: *Opt. Express* 18.12 (2010), pp. 12552–12561. DOI: 10.1364/OE.18.012552. URL: <http://www.opticsexpress.org/abstract.cfm?URI=oe-18-12-12552>.
- [18] Shan Shan Kou et al. “Transport-of-intensity approach to differential interference contrast (TI-DIC) microscopy for quantitative phase imaging”. In: *Opt. Lett.* 35.3 (2010), pp. 447–449. DOI: 10.1364/OL.35.000447. URL: <http://ol.osa.org/abstract.cfm?URI=ol-35-3-447>.
- [19] Kazuo Ishizuka and Brendan Allman. “Phase measurement of atomic resolution image using transport of intensity equation”. In: *Journal of electron microscopy* 54.3 (2005), pp. 191–197.
- [20] KA Nugent et al. “Quantitative phase imaging using hard x rays”. In: *Physical review letters* 77.14 (1996), pp. 2961–2964.

- [21] D. Paganin and K. A. Nugent. “Noninterferometric Phase Imaging with Partially Coherent Light”. In: *Phys. Rev. Lett.* 80 (12 1998), pp. 2586–2589. DOI: 10.1103/PhysRevLett.80.2586. URL: <http://link.aps.org/doi/10.1103/PhysRevLett.80.2586>.
- [22] Jonathan Petrucci, Lei Tian, and George Barbastathis. “The transport of intensity equation and partially coherent fields”. In: *Biomedical Optics*. Optical Society of America. 2012.
- [23] Adam M Zysk et al. “Transport of intensity and spectrum for partially coherent fields”. In: *Optics letters* 35.13 (2010), pp. 2239–2241.
- [24] Aamod Shanker et al. “Analysis of edge effects in attenuating phase-shift masks using quantitative phase imaging”. In: *Proc. SPIE* 8880 (2013), 88802A–88802A–12. DOI: 10.1117/12.2027825. URL: <http://dx.doi.org/10.1117/12.2027825>.
- [25] Kenji Yamazoe and Andrew R. Neureuther. “Modeling of through-focus aerial image with aberration and imaginary mask edge effects in optical lithography simulation”. In: *Appl. Opt.* 50.20 (2011), pp. 3570–3578. DOI: 10.1364/AO.50.003570. URL: <http://ao.osa.org/abstract.cfm?URI=ao-50-20-3570>.
- [26] M. Beleggia et al. “On the transport of intensity technique for phase retrieval”. In: *Ultramicroscopy* 102.1 (2004), pp. 37–49. ISSN: 0304-3991. DOI: <http://dx.doi.org/10.1016/j.ultramic.2004.08.004>. URL: <http://www.sciencedirect.com/science/article/pii/S0304399104001664>.
- [27] T. E. Gureyev, A. Roberts, and K. A. Nugent. “Partially coherent fields, the transport-of-intensity equation, and phase uniqueness”. In: *J. Opt. Soc. Am. A* 12.9 (1995), pp. 1942–1946. DOI: 10.1364/JOSAA.12.001942. URL: <http://josaa.osa.org/abstract.cfm?URI=josaa-12-9-1942>.
- [28] Jelena A. Schmalz et al. “Phase retrieval using radiation and matter-wave fields: Validity of Teague’s method for solution of the transport-of-intensity equation”. In: *Phys. Rev. A* 84 (2 2011), p. 023808. DOI: 10.1103/PhysRevA.84.023808. URL: <http://link.aps.org/doi/10.1103/PhysRevA.84.023808>.
- [29] Jorge Nocedal and Stephen J Wright. *Conjugate gradient methods*. Springer, 2006.
- [30] R. A. Budd et al. “Development and application of a new tool for lithographic mask evaluation, the stepper equivalent Aerial Image Measurement System, AIMS”. In: *IBM Journal of Research and Development* 41.1.2 (1997), pp. 119–129. URL: <http://dx.doi.org/10.1147/rd.411.0119>.
- [31] Kenny K. Toh and Andrew R. Neureuther. *Identifying And Monitoring Effects Of Lens Aberrations In Projection Printing*. 1987. DOI: 10.1117/12.967051. URL: <http://dx.doi.org/10.1117/12.967051>.
- [32] Mats GL Gustafsson. “Surpassing the lateral resolution limit by a factor of two using structured illumination microscopy”. In: *Journal of microscopy* 198.2 (2000), pp. 82–87.

- [33] Pierre Bon et al. “Quadriwave lateral shearing interferometry for quantitative phase microscopy of living cells”. In: *Opt. Express* 17.15 (2009), pp. 13080–13094. DOI: 10.1364/OE.17.013080. URL: <http://www.opticsexpress.org/abstract.cfm?URI=oe-17-15-13080>.
- [34] Timm Weitkamp et al. “X-ray phase imaging with a grating interferometer”. In: *Optics express* 13.16 (2005), pp. 6296–6304.
- [35] A. Barty et al. “Quantitative optical phase microscopy”. In: *Opt. Lett.* 23.11 (1998), pp. 817–819.